POLITECNICO DI TORINO
Repository ISTITUZIONALE

Praseodymium Doping in Ceria-supported Palladium Nanocatalysts as an Effective Strategy to Minimize the Inhibiting Effects of Water During Methane Oxidation

Original
Praseodymium Doping in Ceria-supported Palladium Nanocatalysts as an Effective Strategy to Minimize the Inhibiting Effects of Water During Methane Oxidation / Ballauri, Sabrina; Sartoretti, Enrico; Hu, Min; D'Agostino, Carmine; Ge, Zijuan; Wu, Liang; Novara, Chiara; Giorgis, Fabrizio; Piumetti, Marco; Fino, Debora; Russo, Nunzio; Bensaid, Samir. - In: APPLIED CATALYSIS. B, ENVIRONMENTAL. - ISSN 0926-3373. - ELETTRONICO. - 320:(2023), p. 121898. [10.1016/j.apcatb.2022.121898]

Availability:
This version is available at: 11583/2971360 since: 2022-09-16T14:39:31Z

Publisher:
Elsevier

Published
DOI:10.1016/j.apcatb.2022.121898

Terms of use:

This article is made available under terms and conditions as specified in the corresponding bibliographic description in the repository

Publisher copyright
Elsevier postprint/Author's Accepted Manuscript

© 2023. This manuscript version is made available under the CC-BY-NC-ND 4.0 license http://creativecommons.org/licenses/by-nc-nd/4.0/.The final authenticated version is available online at: http://dx.doi.org/10.1016/j.apcatb.2022.121898

(Article begins on next page)

08 September 2024

Praseodymium doping in ceria-supported palladium nanocatalysts as an effective strategy to minimize the inhibiting effects of water during methane oxidation

Sabrina Ballauri[a], Enrico Sartoretti[a], Min Hu[b], Carmine D'Agostino[b,c], Zijuan Ge[d], Liang Wu[d], Chiara Novara[a], Fabrizio Giorgis[a], Marco Piumetti[a], Debora Fino[a], Nunzio Russo[a] and Samir Bensaid[a,*]

[a] Department of Applied Science and Technology, Politecnico di Torino, Corso Duca degli Abruzzi, 24, 10129 Turin, Italy.

[b] Department of Chemical Engineering, The University of Manchester, Oxford Road, Manchester M13 9PL, UK

[c] Department of Civil, Chemical, Environmental and Materials Engineering, Alma Mater Studiorum – Università di Bologna, Via Terracini, 28, 40131 Bologna, Italy

[d] School of Chemistry and Materials Science, University of Science and Technology of China, Hefei Anhui, 230026, P.R. China

* Corresponding author:

E-mail address: samir.bensaid@polito.it (S. Bensaid).

ABSTRACT

The present study reports an improved design for Pd/Ce-Pr catalysts. Pd-impregnated nanostructured ceria-praseodymia catalysts with different compositions were comprehensively characterized and tested for dry and wet methane oxidation. The strong PdO-PrO_x interactions, detected via XRD, TPR/TPO, Raman and HRTEM analyses, retain Pd mainly in its oxidized form in the materials with high praseodymium content, thus resulting in a lower activity. Conversely, the introduction of a limited amount of Pr in ceria allows to obtain a more active catalyst (2% of Pd supported on a mixed oxide with 10% of Pr) than the typical Pd/CeO_2 systems. Hence, the simultaneous presence of Pd in its reduced and oxidized forms results to be a key factor for high activity. Additionally, the higher hydrophobicity of this sample, investigated through NMR and *in situ* FTIR, markedly reduces the H_2O inhibition effect typical of Pd-based materials, paving the way for using this system in real applications.

Keywords: Catalytic methane oxidation; Palladium/ceria-praseodymia catalysts; Doped ceria; Hydrophilicity-hydrophobicity; Water inhibition

1. Introduction

Methane oxidation on palladium-containing materials has been widely studied with regard to their high catalytic activity [1–3]. In this context, the palladium deposition on different supports and the advancement of synthesis procedures have enabled the achievement of high-performance systems which exhibit high activity at low temperature and retain their high activity as well as stability at high temperature.

Against this backdrop, Pd@CeO_2 structures, composed by a palladium core surrounded by a ceria shell [4,5], or the amorphous mixed palladium-ceria phase which covers the ceria crystallites obtained through the ball-milling method [6] have recently attracted considerable attention due to the intimate contact between the palladium species and a redox active support.

However, from an application perspective, efforts are still needed to improve the activity of palladium-based catalysts in the presence of water. As a matter of fact, water vapour is commonly present in large quantities (5-15%) for applications related to emissions control catalysis. Despite steam has been proved to promote the formation of grain boundaries in Pd nanoparticles [7], which are highly active defect sites, water has an overall detrimental effect on the performances of palladium-based materials for methane abatement.

Given its high affinity to palladium species, it is generally accepted that water competitively adsorbs with methane on the surface active sites giving rise to an inactive and stable $Pd(OH)_2$ phase [8]. This adverse effect of water is much more pronounced in the low-temperature range (< 450 °C) [9] and is also confirmed from a kinetic standpoint; the negative reaction order for water (generally equal to -1) [10] gives a glimpse of the distinct surface coverage throughout the methane oxidation reaction.

The detrimental influence of water on Pd-based materials is also affected by the type and nature of the catalytic carrier. Although redox supports appear to be more resistant to the inhibition effect [11], the surface hydroxyl/water accumulation markedly hinders the oxygen exchange at the palladium-support interface, resulting in a drop in catalytic activity [12]. Conversely, for other supports such as alumina, the water absorption capacity seems to positively influence the catalytic performance of the system, at least as regards methane oxidation performed in dry conditions. A high affinity between water and support has proven to lower the local presence of water in the proximity of Pd active sites, keeping their activity undamaged [13,14]. However, the system loses part of its effectiveness if water is present in the reactor inlet flow and that is why, according to the latest findings by Huang et al. [15], *in situ* water sorption systems (stronger water sorbents, e.g., CaO mixed with the catalyst) resulted to be a well-functioning strategy to maintain a high reaction rate also in the presence of water.

With this knowledge, considering the well-known ability of CeO_2 to enhance the Pd redox properties [3] and the ability of PrO_x to retain the noble metals in their oxidized form [16,17], we investigated the Pd deposition on nanostructured Ce-Pr oxides with different compositions. In particular, we comprehensively characterized these novel materials and tested them in dry and wet CH_4 oxidation. Also, the different water-catalyst and hydrocarbon-catalyst interaction strengths were evaluated in order to move the studies towards hydrophobic systems able to minimize the competitive H_2O and CH_4 adsorption on the surface of the catalysts and, therefore, reduce the well-established water inhibition effect.

2. Experimental

2.1 Catalyst synthesis

Nanostructured ceria, ceria-praseodymia and praseodymia supports for palladium nanoparticles were synthesised through hydrothermal synthesis. As far as the support preparation is concerned, appropriate amounts of $Ce(NO_3)_3{\cdot}6H_2O$ (Sigma-Aldrich, 99.99% purity) and $Pr(NO_3)_3{\cdot}6H_2O$ (Sigma-Aldrich, 99.9% purity) were dissolved in 9 mL of deionized water to obtain 20 mmol of total cations in the resulting solution, the two cations being in a proportion equal to the desired one in the final oxide. It is worth reminding that trace impurities of lanthanides may be present in Ce/Pr oxides precursors and hence in the final catalysts, with possible implications on their structural and physico-chemical properties. At the same time, a second basic solution was made by dissolving 48 g of NaOH (Sigma-Aldrich, 98% purity) in 70 mL of deionized water. At this point, the nitrate solution was added dropwise to the basic one, maintaining the system under continuous stirring. The opacification of the solution and the formation of a pale brown slurry were observed at the moment of contact between the lanthanide-water drop and the NaOH solution. The obtained slurry was maintained under stirring at room temperature for 1 h and afterwards transferred into a stainless-steel autoclave with inner Teflon-liner to undergo an aging treatment at 180 °C for 24 h. Subsequently, the precipitate was recovered through different centrifugation cycles and washed with ethanol and deionized water several times until a pH close to 7 was obtained, in order to remove as much as possible the NaOH traces. The wet solid was then dried at 60 °C overnight. Finally, the dried powder was gently crushed in a mortar to eliminate the largest granules and then calcined at 650 °C for 4 h.

Palladium-based catalysts containing 2 wt% of noble metal were prepared via incipient wetness impregnation. In detail, 1.5 g of each support was put in a ceramic crucible, placed on a heating plate, and gradually heated to 150 °C.

Subsequently, the materials were impregnated by using an aqueous solution of $Pd(NO_3)_2$. Lastly, the catalysts were calcined in air at 900 °C for 4 h.

Throughout this work, the supports and the palladium-based catalysts were respectively labelled as Ce(100-X)Pr(X) and Pd/Ce(100-X)Pr(X), wherein X stands for the nominal atomic percentage of praseodymium in the sample on a Ce + Pr basis (X = 0, 10, 25, 50 and 100).

2.2 Catalyst characterization

Nitrogen physisorption at -196 °C was conducted with a Micromeritics Tristar II 3020 instrument for the determination of the surface area of the samples. Before the measurement, the materials were pre-treated at 200 °C for 2 h in a nitrogen flow for outgassing water and/or other physisorbed contaminants present on the surface of the samples. The surface area was evaluated by using the Brunauer-Emmett-Teller (BET) method.

Powder X-ray diffraction (XRD) was carried out through a Philips X'Pert PW3040 diffractometer using a Cu Kα radiation characterized by a wavelength of 1.5419 Å. The measure was performed with a 2θ angle ranging from 20 to 80°, a step size of 0.013° and an acquisition time of 0.2 seconds per step. The peaks were attributed consulting the Powder Diffraction Files by the International Centre of Diffraction Data (ICDD). The lattice parameter (a) of the different catalysts was evaluated by employing the Nelson-Riley extrapolation method, whereas the crystallites dimension was calculated through the Debye-Scherrer formula: $D = k \cdot \lambda / (b \cdot \cos\theta)$ where k is a constant depending on the crystallites sphericity, assumed equal to 0.9, λ is the wavelength of the incident beam, b is the peak width at mid-height (FWHM) and θ is the diffraction angle. The peak broadening was corrected by using a lanthanum hexaboride (LaB_6) crystal as a standard reference.

The proper composition of the Pd-containing samples was checked out through inductively coupled plasma-mass spectrometry (ICP-MS) performed in a Thermo Scientific iCAP RQ ICP-MS apparatus. Catalysts were digested at 200 °C for 0.5 h in a mixture of nitric and hydrochloric acid together with hydrogen peroxide and finally diluted until reaching the proper metal concentration for the measurements.

Raman analysis was carried out in a Renishaw InVia micro-Raman spectrometer, using a 514.5 nm excitation wavelength and a CCD detector. For each sample, three room temperature spectra were collected in different points, using a 5x objective and an acquisition time of 225 s. *In situ* Raman measurements were performed in a Linkam TS1200 PID-controlled cell.

Catalyst morphology was investigated using a Zeiss Merlin field-emission scanning electron microscope (FESEM) with a Gemini-II lens column. The high-resolution transmission electron microscopy (HRTEM) images were collected on a JEM 2100F field emission transmission electron microscope operated at an accelerating voltage of 200 kV. The HRTEM images were analysed using a fast Fourier transform (FFT) method. Morphology and microstructure of catalysts were also investigated with a high-angle annular dark-field scanning transmission electron microscopy (HAADF-STEM) on JEM-2100F (with Oxford X Max EDS system) instrument with an electron acceleration energy of 200 kV.

The chemical state of the elements present in the Pd-based catalysts was studied via X-ray photoelectron spectroscopy (XPS). Measurements were carried out on an XPS PHI 5000 Versa Probe apparatus, using a bandpass energy of 187.85 eV, a take-off angle of 45° and a diameter of the X-ray spot size of 100.0 µm. Data analysis was performed using Casa XPS software and the binding energy of the XP spectra was referenced to the C 1s peak at 284.8 eV. The reliability of the deconvolution procedure was verified by applying the Monte Carlo procedure.

The reducibility of the materials and, therefore, their redox properties were analysed through temperature-programmed reduction employing hydrogen as reducing molecule (H_2-TPR). The analysis was performed in a Thermo Scientific TPDRO 1100 with a TCD detector keeping the sample (50 mg) in a 20 mL min^{-1} flow of 5 vol% H_2 in Ar. Afterwards, the system was heated from 50 to 900 °C with a ramp of 10 °C min^{-1}. Prior to analysis, a thermal treatment was performed exposing the catalysts to a 20 mL min^{-1} flow of oxygen at 550 °C for 1 h.

Temperature programmed oxidation (TPO) analysis was carried out in a quartz U-shaped reactor using 120 mg of catalyst placed on a quartz wool bed. The reactor was located in a PID-controlled furnace and the tests were performed by fluxing a mixture of 2% of oxygen in N_2 with a total flowrate of 50 mL min^{-1}. Three heating/cooling cycles were performed for each sample to stabilize the behavior of the high-temperature PdO-Pd transition; the third cycle was regarded as representative of the TPO tests. In particular, for each cycle, the system was heated up to 900 °C and then

cooled to 200 °C with a ramp of 10 °C min^{-1}. The TPO analysis was conducted for both supports and Pd-containing materials, so allowing to discriminate the O_2 release/uptake by either palladium or catalytic carriers; the detailed procedure is described in the supporting information (SI) document. The O_2 concentration leaving the reactor was monitored through an Emerson XStream X2GP paramagnetic oxygen analyzer. The chemical state at the beginning of the third heating cycle was investigated through *ex situ* XPS analyses. In detail, the experiments were blocked at 200 °C by switching the O_2–N_2 flow with pure N_2. Once the oxygen concentration was equal to zero, the system was cooled down as quickly as practicable, and the catalyst was picked up and subjected to XPS analyses.

Fourier transform infrared spectroscopy (FTIR) was carried out by using a Bruker Invenio S spectrometer fitted out with an MCT detector. Spectra were recorded in transmittance mode in the region ranging from 4000 to 800 cm^{-1} at a spectral resolution of 2 cm^{-1}. Samples were assembled in self-supporting pellets (with an apparent density of ~ 30 mg cm^{-2}) pressing the materials at 4.5 tons; then, they were directly placed in the quartz IR cell. Once a room-temperature spectrum was acquired, each sample was degassed at 10^{-4} mbar at different temperatures by connecting the IR cell to a high vacuum line. In particular, spectra were acquired after treating the materials at 150, 300 and 500 °C for 1 h and subsequently cooling the system to room temperature. *In situ* FTIR measurements were conducted to study the material hydrophilicity/hydrophobicity properties, by admitting water into the IR cell. In detail, after an under-vacuum pretreatment (10^{-4} mbar) at 500 °C for 1 h and the subsequent cooling to room temperature, water was sent to the IR cell reaching a pressure of 11 mbar and progressive degassing was performed firstly under controlled pressure, then over time (after reaching the minimum achievable pressure).

NMR relaxation measurements were performed on a Magritek SpinSolve benchtop spectrometer operating at a ^1H frequency of 43 MHz. The spin lattice relaxation time (T_1) was measured using the inversion recovery pulse sequence [18] and the transverse relaxation time (T_2) was measured with the CPMG (Carr-Purcell-Meiboom-Gill) pulse sequence [19]. T_1 measurements were performed varying the time delay between 0.1 s and 10 s. T_2 measurements were performed using an echo time of 120 µs with a number of echoes per step varying in the range 10-2500. A number of sixteen experimental points for T_1 and T_2 measurements were acquired, 16-32 scans were used for each experimental point, with a repetition time equal to the max delay time for T_1 and $5 \times T_1$ for T_2 measurement in all cases. Samples were prepared by soaking catalyst particles in *n*-octane and water separately for at least 48 hours to equilibrate. The saturated solid catalyst samples were then dried on a pre-soaked filter paper to remove the excess solvent on the external surface and transferred to 5 mm NMR tubes. To ensure a saturated atmosphere in the NMR tube, hence minimizing errors due to evaporation of volatile liquids, a small amount of pure liquid was placed onto absorbed filter paper, which was then placed under the cap of NMR tube. The tube was placed into the magnet and left for approximately 20 min to achieve thermal equilibrium before starting the measurements. All the measurements were carried out at atmospheric pressure and room temperature. The typical relative error on the T_1 and T_2 measurements was 2%, giving a combined error of approximately 3% on the T_1/T_2 values.

2.3 Catalytic activity tests

Methane oxidation tests were conducted in a quartz U-tube reactor with a 4 mm inner diameter, heated by a PID-controlled furnace. The temperature inside the reactor was monitored through the insertion of a thermocouple, which was located immediately above the catalytic bed. The latter was prepared by gently mixing 50 mg of catalyst and 150 mg of inert silicon carbide (SiC), then placed in the U-reactor on a quartz wool bed. The utilization of the silicon carbide proved to be fundamental to avoid localized increase in temperature. Before starting the analysis, the samples were pre-treated in air at 100 °C for 30 min in order to remove physisorbed compounds on the material surface. Oxidation tests were performed by exposing the catalytic mixture to a flow of 0.3 vol% CH_4 and 1.2 vol% O_2 balanced with nitrogen, using a constant flow rate of 150 mL min^{-1}, which corresponds to a gas hourly space velocity (GHSV) between 60000 and 80000 h^{-1} (the same mass of catalysts was used in all the tests, but samples richer in praseodymium were characterized by a lower bulk density). The wet condition tests were performed through a Bronkhorst Controlled Evaporation and Mixing (CEM) apparatus by adding 5 vol% of water to the flow entering the reactor. At the reactor outlet, the CH_4, CO, CO_2 and O_2 concentrations were tracked in an ABB AO2020 non-dispersive infrared analyser and an Emerson XStream X2GP paramagnetic oxygen analyser. Lastly, for stabilization reasons, in each experiment two heating and cooling cycles were conducted by increasing the temperature up to 950 °C and bringing it back to 100 °C, using a ramp of 5 °C min^{-1}.

Long-term stability tests in the presence of water were carried out performing a first complete methane oxidation cycle and blocking the second run at the temperature of interest for different hours.

Ex situ XPS analyses were carried out after blocking the dry or wet CH4 oxidation at different temperatures, in order to study the chemical state of the materials at conditions other than room temperature, using a procedure similar to that described for the TPO experiments.

3. Results and discussion

3.1 Catalyst textural and structural properties

Table 1. Textural properties of powder materials resulting from N_2 physisorption, X-ray diffraction, ICP-MS and Raman measurements.

Sample	**S_{BET}**[a] ($m^2\ g^{-1}$)	**D_c**[b] (nm)	**Pd content**[c] (wt%)	**Ce-to-Pr molar ratio**[c]	**D/F_{2g} ratio**[d]
Pd/Ce100	4.1	289	1.59	-	0.05
Pd/Ce90Pr10	5.6	222	1.64	9.00	1.28
Pd/Ce75Pr25	5.7	73	1.74	3.06	2.27
Pd/Ce50Pr50	7.2	50	1.53	1.03	4.14
Pd/Pr100	2.6	110	2.19	-	-

[a]Surface area obtained via BET method (error below 0.12 $m^2\ g^{-1}$).
[b]Average size of ceria-based crystallites evaluated employing Scherrer's equation.
[c]Obtained through ICP-MS.
[d]Calculated from Raman spectra

Table 1 lists the primary structural properties of the Pd-based materials. As far as the surface area is concerned, its value is quite small and ranges from 4.1 to 7.2 $m^2\ g^{-1}$. Specifically, starting from Pd/Ce100, a rise in the S_{BET} measure was noted when increasing the praseodymium content in the catalytic framework. Such a trend, ascribed to the ability of praseodymium to modify the textural properties of ceria, is in line with prior studies [16,20]. A fairly low value (2.6 $m^2\ g^{-1}$) was instead observed as a result of the palladium impregnation on pure praseodymium oxide. In general, the surface area of Pd-containing materials turned out to be lower than that of the corresponding supports (Table S1) and the surface area reduction was due to the natural sintering phenomenon occurring during the high-temperature calcination. Again with reference to Table 1, ICP-MS analysis revealed an actual palladium loading of about 1.6 wt% for all the Pd/Ce-containing materials and 2.19 wt% for Pd/Pr100, thus rather similar to the nominal one. Additionally, the same applies to the cerium-to-praseodymium ratio, confirming the proper composition of the investigated samples.

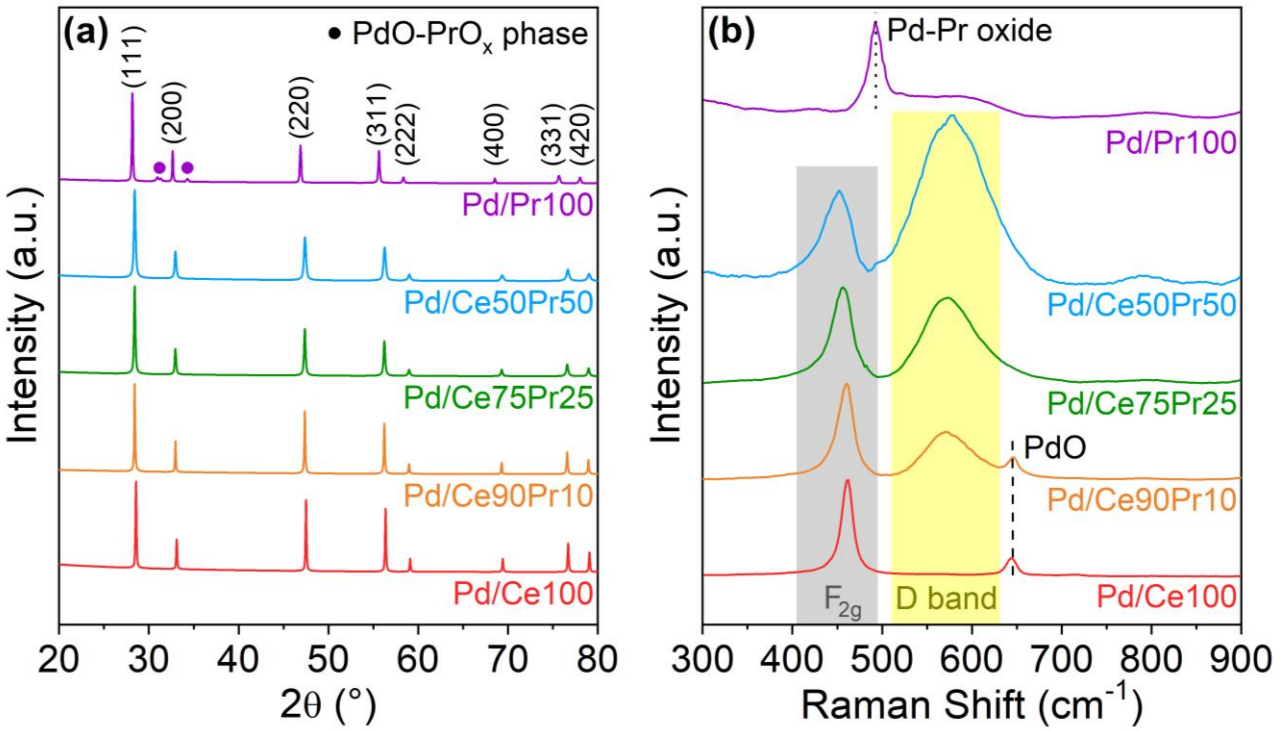

Fig. 1. X-ray diffractograms (a) of powder palladium-impregnated catalysts normalized with respect to the most intense peak of Ce-Pr oxide. Room temperature Raman spectra (b) of the Pd-impregnated catalysts, normalized to the intensity of the F_{2g} peak (of the most intense peak for Pd/Pr100).

Fig. 1a shows the powder X-ray diffractograms of Pd-impregnated catalysts, whereas the XRD patterns of the supports are displayed in Fig. S1. The presence of (111), (200), (220), (311), (222), (400), (331) and (420) planes in the X-ray diffractograms, in both supports and impregnated samples, clearly marks the presence of the typical fluorite structure of ceria and ceria-praseodymia catalysts [21]. Furthermore, double peaks arising from the segregation of cerium and praseodymium oxides were not observed in any sample. Considering that cerium and praseodymium ions are characterized by very similar ionic radii, the latter point suggests the formation of a solid solution between the two oxides even upon the introduction of a large amount of dopant into the ceria lattice. As illustrated in Fig. 1a, no peaks due to the presence of palladium oxide or metallic palladium were observed in all the diffractograms. Although their rather low surface area, these supports seem to promote a good palladium dispersion avoiding the segregation of large PdO or Pd clusters detectable through a standard XRD analysis. Moreover, it is worth noting that three peculiar peaks centred at 30.9, 31.3 and 34.3° were observed in the diffraction pattern of the Pd/Pr100 sample (purple line in Fig. 1a). According to Chou et al. [22], these peaks can be related to the formation of a palladium-praseodymium binary oxide, arising from the high-temperature calcination.

X-ray diffraction also evidenced the presence of large crystallites in the samples, with average dimensions ranging from 50 to 289 nm (Table 1). In detail, as to the Pd-impregnated ceria and Ce-Pr mixed oxides, the higher is the Pr content in the ceria structure, the more the crystallite size decreases. Such an effect was also observed in the bare supports (see Table S1) and is in agreement with the surface area increase obtained by adding praseodymium to the catalytic framework. The crystallite size reduction in doped ceria can be ascribed to partial Pr segregation at the boundaries of the nanocrystalline domains, thereby hindering their growth. Moreover, the simultaneous presence of Pr^{4+}/Pr^{3+} at the crystallite edges can result in the formation of preferential pathways for oxygen diffusion, with the subsequent increase of oxygen mobility in the oxide framework [23]. On the other side, Pd/Pr100 exhibits instead an intermediate crystallite dimension as compared with that observed for Pd-impregnated ceria-praseodymia samples. Moreover, comparing Tables 1 and S1 shows that the crystallite size of palladium-containing catalysts is greater than that of supports as an outcome of the calcination treatment at 900 °C. This result is consistent with the BET surface area decrease previously discussed.

The structural properties of the catalysts were further explored by means of Raman spectroscopy. The Raman spectra of the Pd-impregnated samples are displayed in Fig. 1b, while those of the supports are shown in Fig. S2a. Cerium oxide is typically characterized by an intense F_{2g} peak at about 465 cm^{-1}, ascribed to the Ce–O stretching mode in the fluorite lattice [24]. This component is present in the spectra of all the Ce-containing samples, suggesting that high amounts of praseodymium can be incorporated in ceria structure. Nevertheless, the F_{2g} peak exhibits gradual red-shift and asymmetric broadening upon Pr addition, revealing an increasing structural distortion consistent with the insertion of Pr ions into ceria lattice [25].

Beside the main F_{2g} mode, a Raman band related to the presence of structural defects in the CeO_2 framework (D band) can be detected in the 550 – 600 cm^{-1} region. The D band of pure ceria has a very low intensity and consists of a sole component centred around 595 cm^{-1}, assigned to intrinsic anionic Frenkel pairs [24] (a magnification of this band is reported in Fig. S2b). After Pd deposition and high temperature calcination, a defect component can be detected at 570 cm^{-1}, related to the presence of oxygen vacancies [26] and probably linked to an increased degree of reduction of the catalyst (Fig. S2b). The Pr-doped samples are characterized by a much more intense defect band, which points out the formation of numerous extrinsic defects in the ceria matrix (e.g. Frenkel sites and oxygen vacancies linked to the incorporation of Pr^{3+} ions). The defect abundance was estimated by calculating the ratio between the areas of the D band and of the F_{2g} peak [24]; the thus obtained values are reported in Table 1 and S2 for the Pd-containing catalysts and the bare supports, respectively. As expected, the D/F_{2g} ratio shows a notable and progressive rise when the Pr content in ceria increases. However, beside the generation of new vacancies and defects, other two phenomena could contribute to the D/F_{2g} rise as well. In fact, Pr doping is associated with a higher light absorbance, which entails a lower penetration depth of the technique; therefore, the Raman spectrum outlines a more superficial portion of the sample, in which defects and vacancies are usually more abundant. In addition, the signal around 570 cm^{-1} may be enhanced by the resonance Raman effect exhibited by some defect sites containing oxygen vacancies close to Pr^{4+} ions [27].

Interesting insights were gained by comparing the spectra of the Pd-containing catalysts with those collected on the bare supports. First of all, a significant growth of the D/F_{2g} ratio can be noticed after Pd impregnation (see Table 1 and S2), indicating that the formation of defects in the ceria-based supports is fostered by the interactions with palladium, especially in the presence of Pr as a dopant. This outcome is consistent with the metal-support interaction described for Pd-ceria systems [1]. Furthermore, Pd deposition results in the appearance of a peak at 645 cm^{-1} in the Raman spectra of Pd/Ce100 and Pd/Ce90Pr10 (Fig. 1b); this band can be assigned to the B_{1g} mode of PdO [28], thus it reveals the presence of segregated PdO domains in the latter samples. The complete absence of an analogous peak in the spectra of the other catalysts suggests that a higher Pr content might hamper the segregation and the growth of PdO clusters, that even if present could be below the sensitivity threshold of the Raman analysis.

Finally, the Raman spectrum of the Pd/Pr100 sample is featured by a sharp peak located at 493 cm^{-1}. Such a component is absent in the spectrum of the bare Pr100 support, and it only appears after Pd impregnation followed by high temperature calcination, as demonstrated by Fig. S2c. Taking into account that the concurrent presence of Pr and Pd at high temperature is required for the appearance of the Raman peak at 493 cm^{-1}, it can be reasonably ascribed to the presence of a Pd-Pr mixed-phase [22], which was also detected through XRD. As a whole, stronger interactions with the support seem to occur when Pd is deposited onto Pr-richer ceria samples.

3.2 Catalyst morphology

Fig. 2 shows the FESEM (column a) and the HRTEM (columns b and c) images of palladium-based catalysts and, in particular, heading towards the bottom, each line defines a catalyst with an increasing amount of praseodymium. Concerning the FESEM images, as widely described in the literature [21,29], the hydrothermal synthesis enables the obtainment of desirable nano-shapes characterized by the exposure of well-defined crystallographic planes and, surprisingly, this morphology is retained also after the Pd-impregnation and the calcination treatment at 900 °C. Nevertheless, as reported in Fig. S3, palladium-containing samples show a more rounded structure compared to the corresponding catalytic carriers. On the whole, Pd/Ce100 exhibits a nanocubic morphology in compliance with the aging treatment at 180°C [29]. Nanofibrous structures start to appear alongside the cubes when increasing the praseodymium percentage in the catalytic framework (> 10%). The elongated particles become predominant in the Pd/equimolar ceria-praseodymia and Pd/pure praseodymia, consistently with the rod-like organization previously observed for nanostructured praseodymium oxides [30].

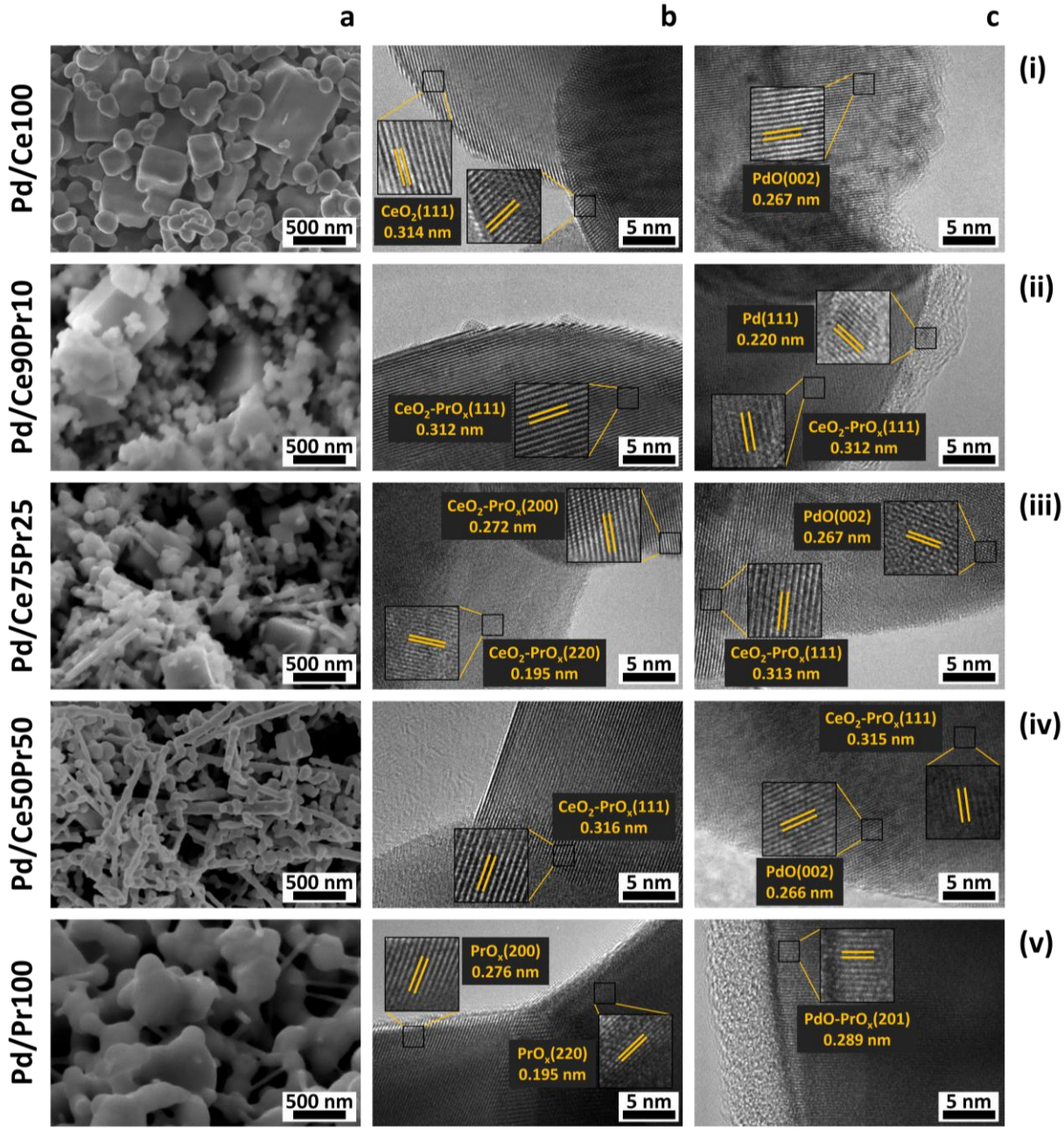

Fig. 2. FESEM (column a) and HRTEM images (columns b and c) of Pd/Ce100 (i), Pd/Ce90Pr10 (ii), Pd/Ce75Pr25 (iii), Pd/Ce50Pr50 (iv) and Pd/Pr100 (v).

Concerning the HRTEM images in Fig. 2, column b provides information about the ceria/praseodymia structure, whereas column c is more focused on the palladium morphology. As far as column b is concerned, starting from the Pd/Ce100 catalyst, the lattice fringes characterized by an interplanar distance of 0.314 nm (Fig. 2-b(i)) were ascribed to CeO_2(111). Conversely, FFT image analysis of Pd/Pr100 (Fig. 2-b(v)) revealed lines with an interplanar distance of 0.276 and 0.195 nm assigned to PrO_x(200) and PrO_x(220), respectively. As regards the cerium-praseodymium mixed oxides, reliably ascribing the observed fringes to a pure oxide or to a mixed phase is not possible, given the high resemblance between ceria and praseodymia in terms of crystal structure. Hence, the partial superficial microsegregation of some CeO_2 or PrO_x domains could not be confirmed nor excluded with certainty. In this regard, additional STEM-EDX mapping analysis pointed out a homogeneous distribution of Ce and Pr in the mixed catalyst particles (see Fig. S4 and Table S3), suggesting that the formation of a single phase appears more likely.

With regards to column c, well-defined palladium nanoparticles were difficult to identify likely due to the impregnation technique which does not allow a homogeneous dispersion of noble metal. Nevertheless, some diversified palladium species were observed in the samples in the form of fringes superimposed on the support framework. In detail,

palladium oxide was detected as PdO(002), with an interplanar distance of 0.266 – 0.267 nm. Some metallic palladium embedded in an amorphous layer surrounding the ceria-praseodymia particles was also noted (a representative example is shown in Fig. 2-c(ii)). Lastly, lattice fringes with an interplanar distance of 0.289 nm were observed in the Pd/Pr100 catalyst (Fig. 2-c(v)). The latter cannot be ascribed to PdO or PrO_x, but they are consistent with the formation of a palladium-praseodymium mixed oxide $Pd_2Pr_2O_5$(201) (Powder Diffraction File PDF: 00-045-0528). As shown in Fig. 3, the Pd/Pr100 sample exhibits a peculiar morphology, marked by sticks-like protuberances with atomic palladium-to-praseodymium ratio approximately equal to 1, in well-agreement with the aforementioned Pd-Pr oxide formula.

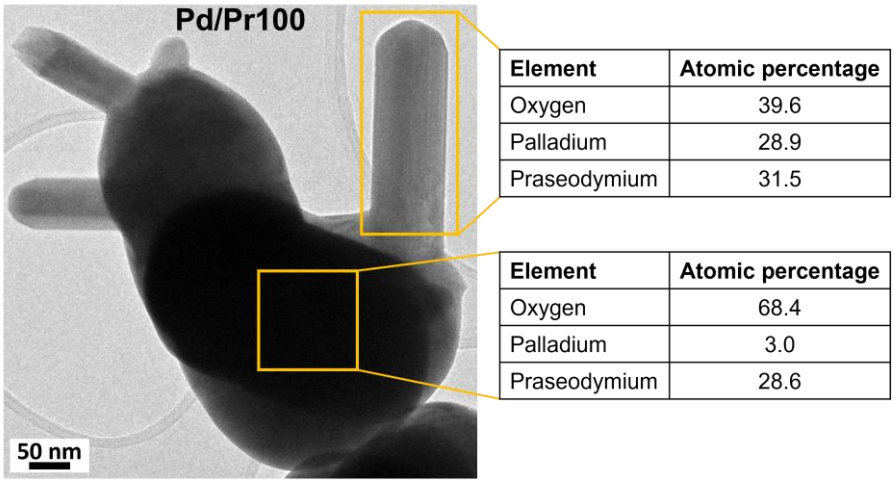

Fig. 3. HRTEM image and energy dispersive X-ray (EDX) microanalysis of Pd/Pr100.

3.3 Catalyst surface composition and chemical state

Table 2. Relative abundance (at%) of oxygen, cerium, praseodymium and palladium species resulting from the XPS spectra deconvolution. The deconvolution errors, reported in Table S4, are low.

Sample	**Oxygen species**		**Ce and Pr reduced ions**		**Palladium species**			
	O_α	O_β	Ce^{3+}	Pr^{3+}	Pd^0	PdO_x	Pd^{2+}	$Pd^{(2+\delta)+}$
Pd/Ce100	34.6	65.4	26.3	-	18.3	37.4	32.2	12.1
Pd/Ce90Pr10	32.8	67.2	21.8	51.3	7.9	23.7	48.4	20.0
Pd/Ce75Pr25	36.6	63.4	19.5	53.7	0.9	18.3	59.1	21.7
Pd/Ce50Pr50	51.0	49.0	18.6	54.9	0.7	15.8	60.1	23.4
Pd/Pr100	62.4	37.6	-	61.6	0.0	15.4	60.8	23.8

Surface-sensitive X-ray photoelectron spectroscopy (XPS) was employed to study the superficial chemical state of palladium-based catalysts. In fact, the oxidation state of oxygen, cerium, praseodymium and particularly of palladium play a key role in the methane oxidation reaction. The relative amounts of the different species detected in each sample are given in Table 2.

As for the oxygen analysis, the O 1s XPS spectra presented in Fig. 4a show two major contributions. The lower binding energy peak (528.5 – 529.2 eV) was ascribed to the O^{2-} anions like those of the crystalline framework, whereas the higher binding energy peak (531.3 – 531.4 eV) was attributed to adsorbed surface oxygen species such as O_2^{2-} and O^- [31]. For the sake of brevity, these two oxygen species were respectively named O_β and O_α. Table 2 shows that the addition of praseodymium to the catalytic structure tends to increase the O_α concentration. Moreover, as a consequence of the praseodymium inclusion, the O_β peaks exhibit a shift towards lower binding energy probably linked to a higher

quantity of charge-reduced ions in the catalytic framework. This result is consistent with the O_β position observed by Zhang et al. [32] for pure praseodymium oxides (binding energy range of 528 – 528.4 eV). Finally, a third peak can be identified in the O 1s spectra of the samples in the binding energy region from 533.6 to 534.6 eV which is commonly assigned to weakly adsorbed species such as OH^- and CO_3^{2-} ions [25]. Although the presence of these groups cannot be ruled out, it should be considered that their decomposition is expected to occur as a consequence of an extended thermal treatment [20]. This additional contribution is more likely related to the overlapping of Pd 3p region; moreover, the peak shift towards higher binding energies reveals that Pd is more reduced in Pd/Ce100 and more oxidized in the Pr-containing materials [33].

The Ce 3d core-level spectra of the samples, shown in Fig. 4c, consist of ten peaks which were categorized into two different groups. The first one matches the $3d_{5/2}$ Ce level and includes the v_o, v, v', v'' and v''' contributions, whereas the second set describes the $3d_{3/2}$ Ce level, and its peaks were denoted u_o, u, u', u'' and u'''. Amongst them, the v_o – u_o and v' – u' pairs were ascribed to Ce^{3+}, while the other six peaks to the Ce^{4+} state [34]. An analysis of Ce 3d XP spectra reveals that cerium is present in both +4 and +3 oxidation states at the catalysts surface, although the most oxidized form prevails in all samples. Moreover, the amount of Ce^{3+} ions decreases as the praseodymium percentage in the catalytic structure increases. In Fig. 4d we also present the Pr 3d core-level spectra of the samples. Even there, three pairs were expected for Pr^{4+} (b''' – a''', b'' – a'' and b – a), while the remaining four (b' – a' and b_o – a_o) were foreseen for the +3 oxidation state [34]. As shown in Table 2, the number of Pr^{3+} ions seems to rise when increasing the dopant concentration in the ceria lattice, as opposed to what was observed in the cerium analysis.

The Pd $3d_{3/2\text{-}5/2}$ spectra are presented in Fig. 4b. As a result of the deconvolution process, the spectra were subdivided into four pairs of peaks linked to palladium species with diversified oxidation states. More specifically, the typical peaks of metallic palladium (marked as Pd^0) were identified at 335.7 and 340.5 eV, whereas those due to the presence of Pd^{2+} (e.g. in segregated palladium oxide domains) appeared at 337.5 and 342.7 eV [35]. Additional peaks at intermediate binding energies (336.7 and 341.7 eV) suggested the presence of palladium ions characterized by an oxidation state between 0 and +2. According to the literature, these peculiar species, defined as surface/interfacial oxides [36] or oxygen-palladium compounds [37], play a pivotal role in palladium oxidation and decomposition processes. They were named as PdO_x (with $x<1$) and may arise either from the contact between PdO and residual metallic palladium particles or from the interaction between metallic Pd and chemisorbed oxygen on the materials surface. Moreover, high binding energy peaks (338.2 and 343.3 eV) were observed in all the samples and assigned to highly oxidized palladium species referred to as $Pd^{(2+\delta)+}$. Such species are commonly ascribed to the formation of a solid solution between the palladium ions and the support through the direct incorporation of the noble metal into the first layers of the carrier structure [38]. The presence of Pd with different oxidation states was also confirmed by a more comprehensive analysis of HRTEM images (Fig. S5). Overall, as illustrated in Fig. 4b and Table 2, all the previously mentioned species can be found in the Pd/Ce100 and Pd/Ce-Pr samples. Nevertheless, as also suggested by the shift of the Pd 3p peak previously discussed, the amount of metallic palladium and PdO_x redox compound significantly decreases with the increase of the praseodymium content in the catalytic structure; at the same time, palladium ions either in the +2 oxidation state or in their strongly oxidized form ($Pd^{(2+\delta)+}$) prevail in catalysts containing a high praseodymium percentage. Overall, it is evident from the results that the praseodymium inclusion enables the conservation of palladium in more oxidized species, i.e. Pd^{2+} and $Pd^{(2+\delta)+}$.

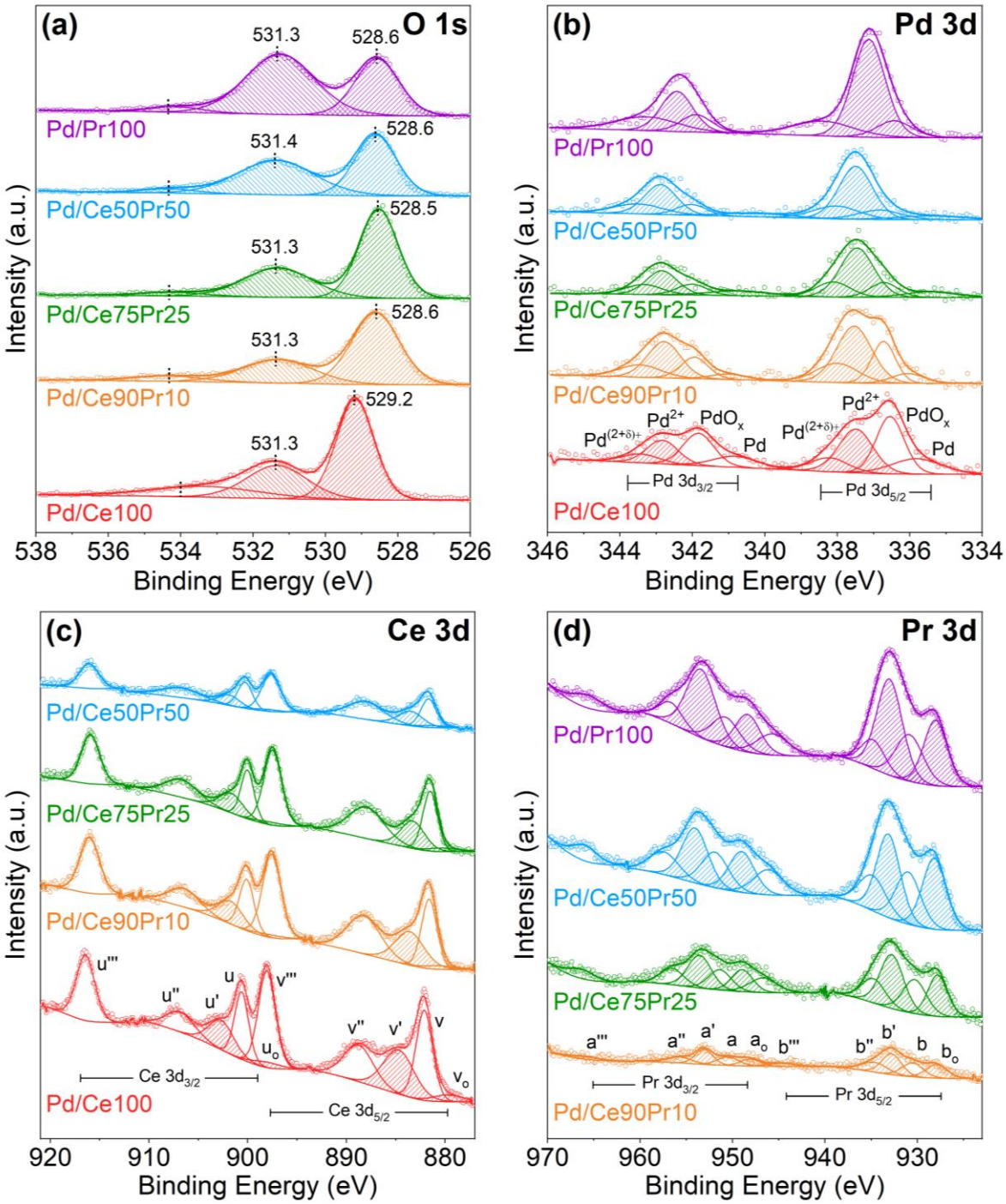

Fig. 4. Deconvoluted high-resolution XPS spectra of powdered palladium-based catalysts in the O 1s (a), Pd 3d (b), Ce 3d (c) and Pr 3d (d) core levels. Dashed peaks highlight the O_α and O_β species in Fig. 4a, the Pd^{2+} species in Fig. 4b, and the +3 cerium and praseodymium oxidation states in Figs. 4c and 4d.

3.4 Temperature programmed experiments

3.4.1 Temperature programmed reduction (H_2-TPR)

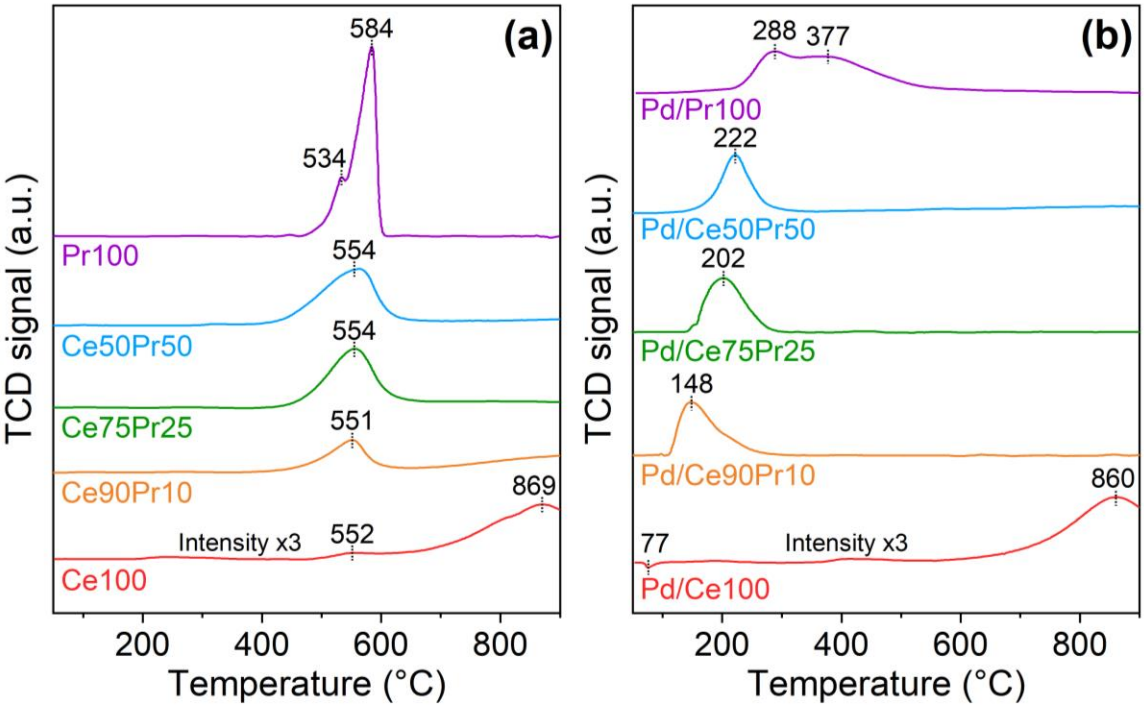

Fig. 5. H_2-TPR profiles of supports (a) and palladium-impregnated catalysts (b) in the extended 50 – 900 °C temperature range.

Fig. 5 shows the results of the H_2-TPR analyses carried out on the palladium-based catalysts and the relative supports. The reduction profiles of the supports are relevant to determine the material change in terms of catalytic reducibility after the palladium impregnation and the calcination at 900 °C. As far as the supports are concerned, the pure ceria profile (red line in Fig. 5a) is distinguished by a low-intensity medium-temperature peak at 552 °C and a growing consumption of hydrogen resulting in a high-temperature peak located at 869 °C. The first contribution is ascribed to the surface oxygen reduction, whereas the second one comes from the bulk oxygen consumption or a part thereof [25]. On the other side, the pure praseodymia reduction profile consists of two partially overlapped reduction peaks centred at 534 and 584 °C. Focusing on Ce-Pr mixed oxides, they exhibit a single peak in an intermediate temperature range (550 – 555 °C) compared to that of cerium and praseodymium oxides. For each sample, the hydrogen uptake was evaluated through the peak area calculation and normalized with respect to the quantity of catalyst used in the test. In this regard, the H_2 consumption is greater in supports constituted by a large quantity of praseodymium (Table S5). Additionally, the percentage of quadrivalent cations (Ce^{4+} + Pr^{4+}) reduced to the trivalent oxidation state was calculated according to Equations S1 and S2. Starting from pure ceria, in which only a small portion of oxide is reduced (15.3%, as per Table S5), the percentage of reduced material grows in the Ce-Pr mixed oxides reaching a maximum value in the pure praseodymia (54.2%, as per Table S5). Thus ultimately, in line with the literature, the surface reducibility of pure ceria at intermediate temperatures is converted into a concurrent reduction of surface and bulk as the praseodymium content in the mixed oxide is increased [20]. The improved reducibility of Pr-doped ceria is likely linked to its high abundance of defect sites and oxygen vacancies, as revealed by Raman spectroscopy, which can promote the oxygen diffusion within the crystal lattice [39].

As a result of the palladium impregnation and the calcination treatment (Fig. 5b), catalysts with different compositions showed different behaviours in terms of reducibility. In detail, the Pd deposition on pure cerium oxide (red line in Fig. 5b) does not change neither the reduction profile obtained for the bare support, nor the hydrogen uptake evaluated throughout the test (Tables 3 and S5). However, the Pd/Ce100 catalyst is probably characterized by a certain reducibility in a temperature range lower than that investigated in these tests (< 50 °C). As a matter of fact, PdO decomposition peaks were detected in the literature at very low temperatures. In this regard, Toso et al. [40] observed two reduction peaks at about 7 °C ascribed to the reduction of highly dispersed PdO_x species and more stable PdO crystals linked to the support. The palladium deposition on praseodymium-containing samples results in a shift of the reduction peaks towards lower temperatures compared to those of the supports. Hence, the introduction of Pd into ceria-praseodymia systems undoubtedly increases their reducibility in terms of lowering the average reduction temperatures

by about 300 – 350 °C. However, it is worth nothing that an increase in the average reduction temperature by increasing the praseodymium content is clearly observable in Fig. 5b. Furthermore, while maintaining the same trend of the supports (higher H_2 consumption for samples richer in Pr), the hydrogen uptake of Pd-based materials is lower compared to that of supports (Tables 3 and S5). Therefore, the noble metal improves the support reducibility but, at the same time, Pr doping seems to inhibit the palladium reduction; nevertheless, the possible reduction of a fraction of PdO below 50 °C is still a possibility that should be considered. Such results compare well with the literature [41] and give a glimpse of the strong interactions between the palladium oxide and the praseodymium-containing supports, as previously observed in XRD and Raman analyses. Lastly, Pd/Ce100 exhibits a negative peak at 77 °C attributed to the β-phase palladium hydride decomposition [42].

Table 3. Hydrogen uptake per gram of samples during the H_2-TPR analysis between 50 and 900 °C.

Sample	**H_2 uptake** (mmol g^{-1})
Pd/Ce100	0.46
Pd/Ce90Pr10	0.56
Pd/Ce75Pr25	0.57
Pd/Ce50Pr50	0.88
Pd/Pr100	1.33

3.4.2 Temperature programmed oxidation (TPO)

TPO analyses were performed to investigate the typical PdO-Pd phase transformation in Pd-based catalysts at high temperature (PdO decomposition to Pd in the heating ramp and subsequent reoxidation of Pd to PdO in the cooling ramp). The latter turns out to be particularly relevant to better understand the palladium redox cycle in the catalytic tests. Considering that these experiments are based on the O_2 release/uptake, the contribution of the support cannot be neglected. The simultaneous presence of abundant defect sites and of the Ce^{4+}/Ce^{3+} and Pr^{4+}/Pr^{3+} redox pairs indeed enhance the oxygen mobility as well as the quantity of removable oxygen from the surface and the bulk of materials (see the H_2-TPR results). Accordingly, the tests were carried out for both Pd catalysts and catalytic carriers; the contribution of the latter was subtracted from the TPO profiles of Pd-containing materials in order to only assess the noble metal redox cycle (detailed procedure in the SI document).

Table 4. O_2 release/uptake during the third TPO cycle and quantitative evaluation of the extent of PdO-Pd phase transition.

Sample	**O_2 release** Heating	**O_2 uptake** Cooling	**PdO→Pd decomposition** (Heating ramp)[a]	**Pd→PdO re-oxidation** (Cooling ramp)[b]
	(mmolO_2 g_{CAT}^{-1})		(%)	(%)
Pd/Ce100	0.041	-0.040	59	57
Pd/Ce90Pr10	0.037	-0.033	52	47
Pd/Ce75Pr25	0.011	-0.011	15	14
Pd/Ce50Pr50	0.007	-0.006	10	8

[a] Percentage of oxidized Pd species reduced to the metallic form during the heating ramp (ratio between the experimental mmolO_2 g_{CAT}^{-1} released during the third heating ramp and the theoretical mmolO_2 g_{CAT}^{-1} if all the oxidized Pd species were reduced to the metallic form)

[b] Percentage of metallic Pd re-oxidized to PdO during the third cooling ramp (ratio between the experimental mmolO_2 g_{CAT}^{-1} uptaken during the third cooling ramp and the theoretical mmolO_2 g_{CAT}^{-1} if the cooling cycle started with the presence of only metallic Pd)

Fig. 6 shows the oxygen release/uptake of Pd species during the third heating/cooling cycle for Pd/ceria-based materials. In detail, focusing on the heating run, the TPO profiles are characterized by an O_2 release peak at a lower temperature (about 740 °C) of approximately equal intensity for all catalysts. In addition, another peak at about 800 °C can be observed for Pd/Ce100 and Pd/Ce90Pr10 and, interestingly, its intensity undergoes a gradual reduction and a shift towards lower temperatures when increasing the dopant percentage into the catalytic structure, merging with the

low temperature peak in the case of Pd/Ce75Pr25. The presence of multiple peaks typically implies diversified oxidized-palladium species or, more likely, different extents of interaction between PdO and supports [36,40]. In line with the literature [22,41], the progressive disappearance of the high-temperature peak suggests the presence of strong interactions between PdO and Ce-Pr oxides, hindering the PdO reduction to the metallic form. As a matter of fact, only the species more weakly linked to the support can be reduced to the metallic form in the 740 – 760 °C temperature range. These outcomes were further demonstrated by evaluating the percentage of oxidized Pd species reduced to metallic Pd and the percentage of Pd re-oxidized throughout the third heating and cooling TPO cycle, respectively. For this calculation, the percentage of oxidized species at the beginning of the third heating cycle was assessed through *ex situ* XPS analyses (comprehensive data in the SI document). As evident in Table 4, in both heating and cooling cycles, the more the Pr percentage increases, the more the fraction of Pd species involved in the PdO-Pd transition decreases. Hence, the introduction of Pr strongly affects the PdO-Pd redox cycle, limiting its extensiveness.

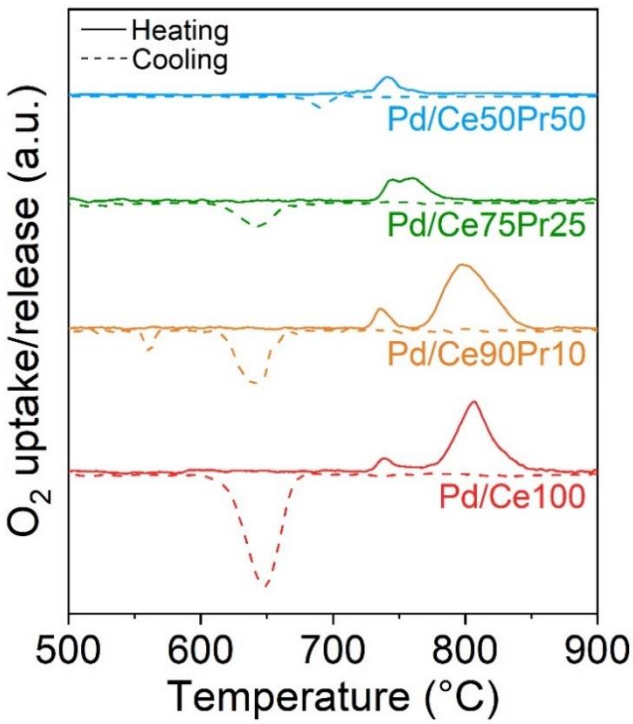

Fig. 6. Oxygen release (solid lines) and uptake (dashed lines) profiles during the third heating and cooling TPO cycle, respectively.

3.3 Extent of water-catalyst and hydrocarbon-catalyst interactions

As anticipated in the introduction, the hydrophilic–hydrophobic features of catalyst surfaces can strongly influence catalytic activity, especially in the presence of water. The latter has indeed a detrimental effect on Pd-containing materials and severely affects their performance in the CH_4 oxidation reaction [8,43].

Therefore, the interactions between water and the surface of the studied materials were investigated via FTIR spectroscopy. In the room temperature spectra of all the fresh catalysts (Fig. S10), it was possible to characterize the water contribution from the OH bending band at 1640 cm^{-1} and the wide band in the 3760 – 2900 cm^{-1} range. The latter includes the OH stretching vibration of physisorbed water along with the OH bending overtone between 3500 and 2900 cm^{-1}. As illustrated in Fig. S10, the intensity of these bands markedly decreased after degassing treatments performed at different temperatures. More specifically, in the H_2O stretching zone, the spectrum recorded after the degassing process at 500 °C turned out to be almost flat in the case of Pd/Ce100 and Pd/Ce90Pr10, whereas the spectrum of Pd/Ce75Pr25 and Pd/Ce50Pr50 was characterized by relevant peaks over the 3659 – 3635 cm^{-1} range due to the presence of bridging hydroxyls [44]. Therefore, it seems that a higher percentage of Pr in the catalytic structure could make the materials more prone to retain adsorbed water on their surface.

In order to better understand these preliminary findings, the interactions of H_2O molecules with the Pd/Ce-Pr surfaces were further studied through *in situ* FTIR spectroscopy. The latter is indeed regarded as a powerful tool to investigate the hydrophilic properties of materials. Hence, after treating the samples under vacuum at 500 °C for 1 h, water was introduced into the IR cell (at a partial pressure of 11 mbar) and a progressive degassing process was performed. FTIR spectra were collected during the degassing phase which was carried out at different pressures (pressure-dependent degassing at 8, 6, 4, 2, 0.8, 0.4 mbar) and 15, 30 and 60 min after reaching the minimum achievable pressure (time-dependent degassing). As detailed in Fig. 7 and Fig. S12, the water-associated bands progressively decreased in intensity during the pressure-dependent degassing for all the catalysts. Strikingly, these bands completely disappeared 15 min after the beginning of the time-dependent degassing for Pd/Ce100 and Pd/Ce90Pr10, while a large amount of adsorbed water was observed for Pd/Ce75Pr25 and Pd/Ce50Pr50 even 60 min after the beginning of the time-dependent degassing process. Therefore, as previously suggested by our preliminary analysis, the samples with greater amount of Pr have more affinity with H_2O than Pd/Ce100 and Pd/Ce90Pr10.

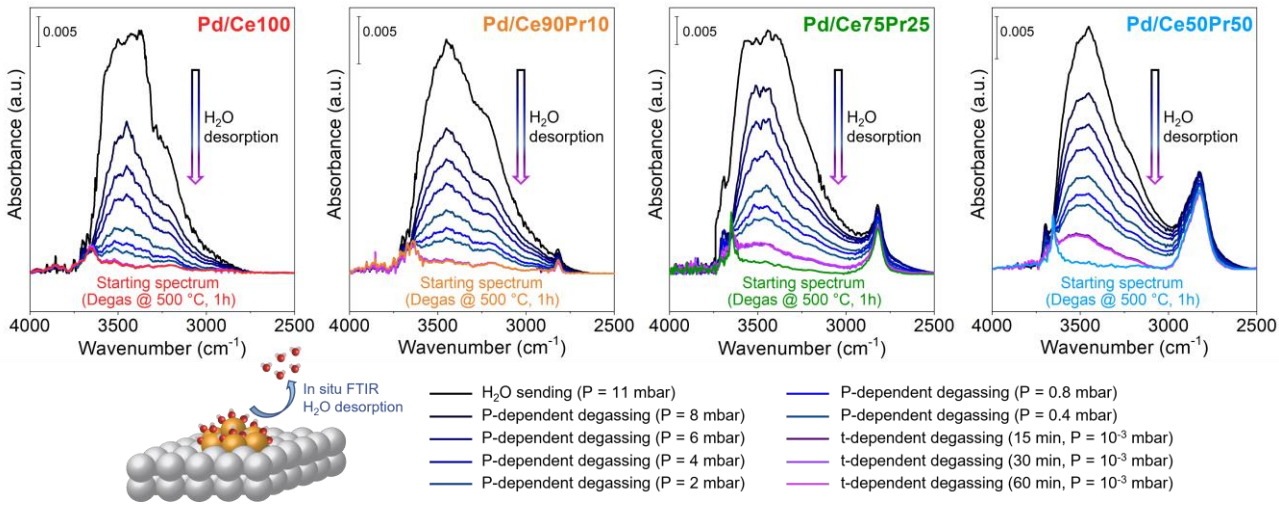

Fig. 7. Baseline subtracted FTIR spectra acquired during the *in situ* water pressure-dependent degassing at P = 11, 8, 6, 4, 2, 0.8, 0.4 mbar and 15, 30, 60 min after reaching the minimum achievable pressure (time-dependent degassing) in the OH stretching region.

The surface properties of the catalysts were further investigated through NMR for the purpose of assessing the interactions of both water and hydrocarbons with the samples. In particular, NMR relaxation time measurements were used to characterize the affinity of water and *n*-octane with the surface of the Pd/Ce-Pr catalysts as a function of Pr content within the Ce-Pr support. From the NMR T_1/T_2 ratio, where T_1 is the longitudinal and T_2 the transverse spin relaxation time, the relative affinity between the selected solvent and the catalyst surface could be determined. Such measurements have previously been used to characterize surface interactions in porous catalysts [45,46], including unravelling the effect of water on the selective catalytic reduction of NO_x using Ag/Al_2O_3 catalysts [47]. A plot of the T_1/T_2 ratio of water versus the Pr percentage for different Pd catalysts (Fig. S13) confirmed the FTIR results. It is evident that the H_2O affinity of the studied samples increases with the increase of the Pr dopant amount in the catalyst structure.

It is now of particular interest to evaluate the T_1/T_2 ratio of *n*-octane normalised over the T_1/T_2 ratio of water as a function of Pr composition (data and fittings for T_1 and T_2 measurements are provided in Supporting Information, Fig. S14 and Table S9). This normalised ratio can be taken as an indicator of the relative surface affinity towards a hydrocarbon as compared to water. A similar approach has previously been used to characterize solvent inhibition over metal nanoparticles supported on porous oxides used in oxidation reactions [48]. As evident from Fig. 8, the addition of 10% Pr leads to a sharp increase in the T_1/T_2 of *n*-octane normalised over that of water. Further increase in Pr loading leads to a gradual decrease of this parameter. These results indicate that small amounts of Pr lead to an increased interaction between the catalyst surface and hydrocarbons. In comparative terms, this could indicate an enhanced adsorption of methane compared to that of water, making the Pd/Ce90Pr10 catalyst more water tolerant.

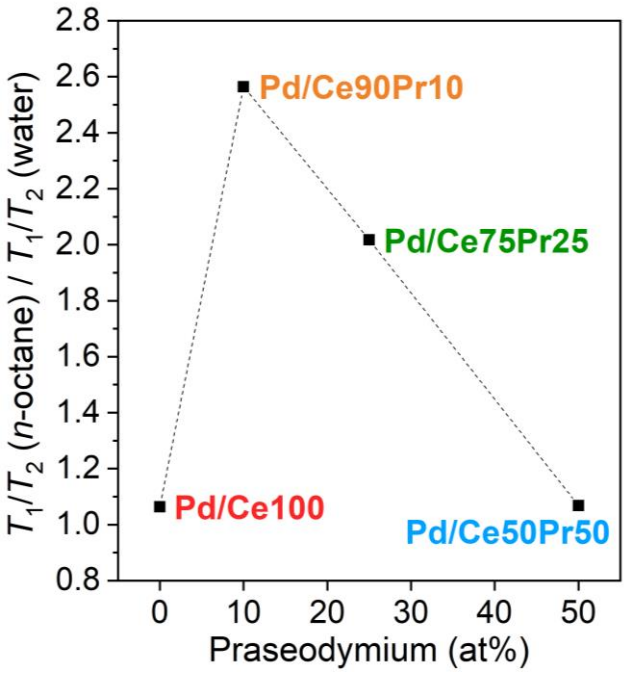

Fig. 8. T_1/T_2 values of *n*-octane normalized over those of water for different Pd-based catalysts as a function of the percentage of praseodymium doping.

3.6 Catalytic activity test

Methane oxidation tests were carried out to evaluate the catalytic activity of the samples. The catalytic performances of palladium-containing materials in both dry and wet conditions are shown in Fig. 9 (Fig. 9a,b for dry tests and Fig. 9c,d for wet tests). For such experiments, the second heating/cooling cycle was recognized as representative of the catalyst behaviour, especially in terms of the PdO/Pd transition (high-temperature PdO reduction to Pd in the heating run and Pd re-oxidation to PdO in the cooling run). For the sake of comparison, we also tested the reaction on the bare supports and the results are illustrated in Fig. S15.

As per the literature [3], looking at the heating run in dry conditions (Fig. 9a), the palladium deposition on pure ceria enables the obtainment of an active catalyst for the methane oxidation reaction. However, this system is characterized by the typical loss of activity in the temperature range of 700 – 800 °C due to the dynamics of the PdO/Pd transformation. Despite having a similar palladium dispersion (see the related assessment method in the SI document), the Pr-containing catalysts exhibit a different behaviour in terms of catalytic activity with respect to that of Pd/Ce100. In detail, the presence of a small percentage of dopant (10%) in the support framework results in two beneficial effects. Firstly, Pd/Ce90Pr10 (orange line in Fig. 9a) exhibits greater activity compared to Pd/Ce100 at both low and high temperatures. Secondly, the typical high-temperature loss of activity due to the thermal decomposition of oxidized palladium species was not observed. Instead, concerning the other compositions, the inclusion of a higher amount of praseodymium in the lattice structure of ceria leads to a considerable decline in the catalytic activity, moving the conversion curves towards higher temperatures. Nevertheless, it should be noted that these highly doped samples, as in Pd/Ce90Pr10, do not show any activity loss in the high-temperature range. An attempt to directly monitor the evolution of the Pd species during the catalysis was made by means of *in situ* Raman spectroscopy (Fig. S18). Unfortunately, limited information was obtained with this technique, due to the absence of Raman signals attributable to metallic Pd and to anharmonicity effects causing a fast disappearance of the PdO features during heating. However, the reduction of part of the initially present PdO during heating in reactive conditions was observed for both Pd/Ce100 and Pd/Ce90Pr10, as can be observed in Fig. S19.

Turning to the cooling run (Fig. 9b), the drop in activity arising from the redox transformation of palladium species appears very pronounced in Pd/Ce100 and its severity decreases as the Pr percentage in the catalytic structure increases. In fact, the activity loss is totally absent in nanostructured Pd/Ce50Pr50 and Pd/Pr100. Thus, as expected by TPO

analyses (as per Fig. 6), the fraction of Pd species in the oxidized form that takes part in the high-temperature redox process markedly decreases with increasing the dopant content embedded in the catalytic framework.

Based on these findings and taking into consideration that the Pd morphology and oxidation state are influenced by the support, we conferred the limited or absent loss of activity at higher temperature of the Pr-based samples to strong interactions of palladium particles with praseodymium oxide, hindering the Pd reduction to the metallic form. Strong PdO-PrO_x interactions were observed in most of the employed characterization techniques (XRD, HRTEM, TPR/TPO and Raman) and result in the formation of a PdO-PrO_x phase in the Pd/Pr100 catalyst. In line with the literature [22], this PdO-PrO_x mixed-phase appears thermally stable in air up to 1200 °C, ahead of its decomposition to the metallic form. A tiny amount of this compound could also be present in the other praseodymium-containing catalysts (Pr < 50%), even though it was not observed with the employed characterization techniques, likely due to the smaller praseodymium quantity. In general, an excessively strong linkage between palladium and praseodymium, as well as the associated retention of the noble metal in the +2 oxidation state (XPS analysis outcomes suggest that the presence of Pr considerably increases the Pd^{2+} stability), seems detrimental for the catalytic activity so as to make the performance of Pd/Ce50Pr50 and Pd/Pr100 equal or even worse than that of the respective supports (Fig. S20).

On the whole, the Pd/Ce90Pr10 catalyst seems to be the best compromise amongst the investigated materials, in terms of Pd-Pr interaction strength. In fact, this catalytic system is highly active at low and medium temperatures, thanks to the presence of Pd in both reduced (i.e. Pd and PdO_x) and oxidized (i.e. Pd^{2+} and $Pd^{(2+\delta)+}$) forms; at the same time, the stabilization of a fraction of Pd^{2+} by praseodymium is responsible for a limited loss of activity due to the PdO-Pd transition at high temperatures.

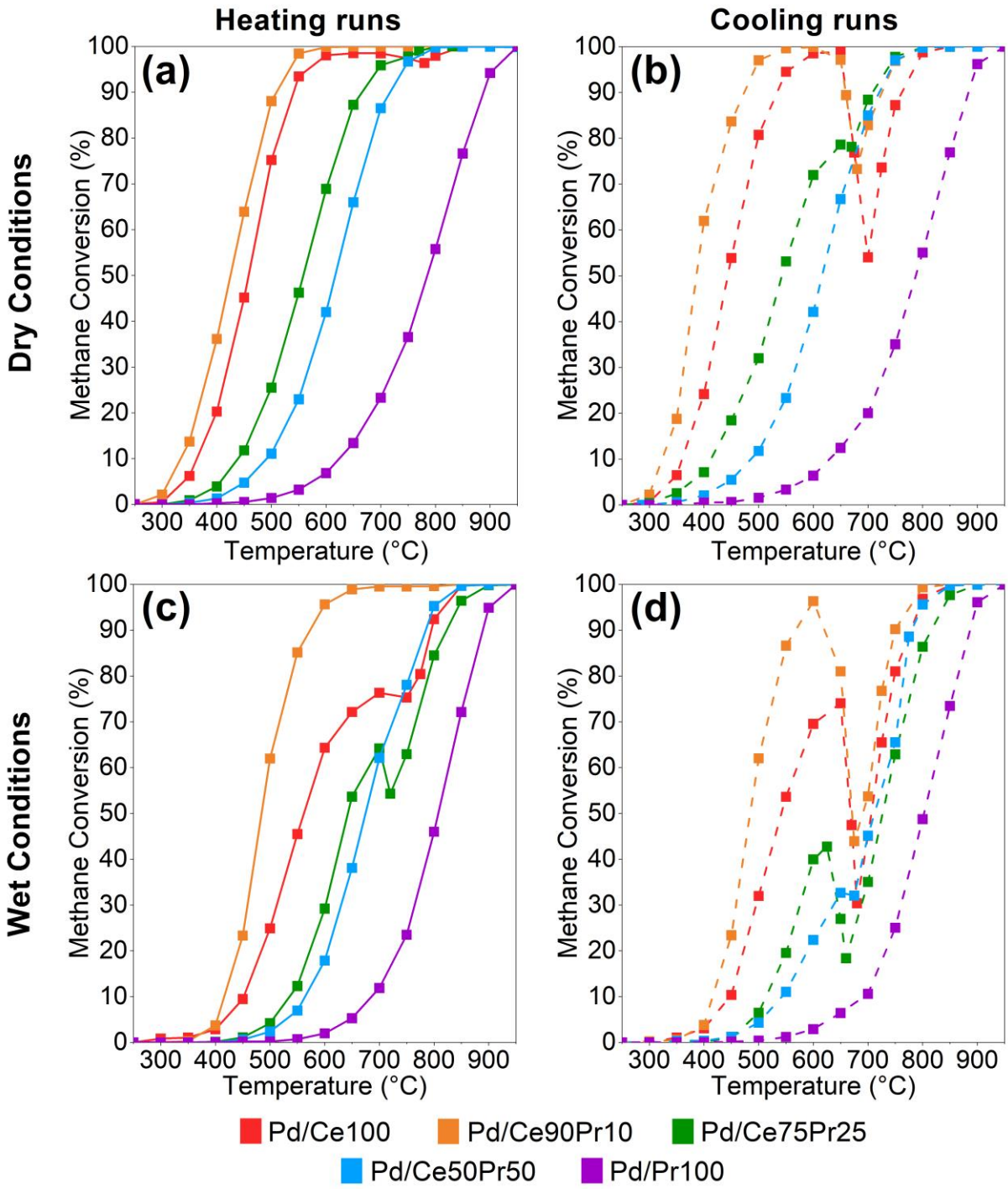

Fig. 9. Methane oxidation light-off curves of Pd/Ce(1-X)Pr(X) materials in dry (a, b) and wet (c, d) conditions. Solid lines (a, c) refer to the second heating run, while dashed lines (b, d) to the second cooling run.

The catalytic performances of palladium-based catalysts were also investigated in wet conditions (5 vol% of water added to the incoming flowrate) in order to study the water inhibition effect. Fig. 9c and Fig. 9d show, respectively, the light-off curves of the second heating and cooling cycle in wet conditions. The addition of water to the feed results in two detrimental effects on the methane oxidation reaction. Firstly, the heating and cooling conversion curves are shifted towards higher temperature (as confirmed by the significantly lower reaction rates reported in Table S16) and, secondly, the presence of water seems to emphasize the high-temperature loss of activity, typical of palladium-based materials. As to Fig. 9c and Fig. 9d, all the catalysts undergo a deactivation effect in the presence of water, at least during the cooling phase. Generally, the medium/high temperature activity of Pd/Ce-Pr samples in the presence of water reflects the one previously observed in dry conditions. Indeed, the activity loss between 650–750 °C progressively decreases with Pr

doping (with the exception of the Pd/Ce75Pr25 sample only during heating, while the expected trend was observed during the cooling run). In addition, the most performing catalyst in dry conditions (Pd/Ce90Pr10) turns out to be exceptionally active also in the presence of water. Its conversion curve is indeed minorly shifted towards higher temperature and does not show the loss of activity in the high temperature range (700 – 800 °C) during heating.

Generally speaking, in these materials the water-induced deactivation may be connected to two major effects [49]: (1) competitive adsorption of water and methane on the palladium active sites and (2) changes in the chemistry of palladium and, in particular, in its oxidation state. As to the first point, water competitively adsorbs on the palladium active sites with the formation of hydroxyl groups strongly bonded to the catalytic surface. The latter detrimentally affects the rate determining step of the CH_4 oxidation reaction, i.e. the C-H bond breakage, especially at medium-low temperature [50]. With this knowledge, the higher affinity with hydrocarbons as compared to water of Pd/Ce90Pr10, highlighted by NMR and FTIR measurements, may account for its superior performances with respect to the other materials. In fact, this property enables a reduction of the competitive adsorption between the water and methane molecules, promoting the methane-catalyst interactions.

As far as the second aforementioned effect is concerned, we studied the evolution of the palladium oxidation state throughout the catalytic tests by means of *ex situ* XPS analyses. More specifically, conventional methane oxidation tests (the second heating/cooling representative cycle, as per usual) were performed, but the reaction was stopped at some temperatures of interest by sending pure nitrogen to the reactor and cooling the system down to room temperature as fast as practicable. In this way, the inert atmosphere allowed to preserve the chemical state achieved by the catalyst at high temperature (as confirmed by *in situ* Raman spectroscopy, see Fig. S19). The powder was thereafter investigated by XPS measurements. Hence, the Pd oxidation state during wet CH_4 oxidation was evaluated for all the samples by stopping the second heating cycle at 675 °C (Fig. S21 is a representative image of the selected breakpoints, while the results coming from the XPS spectra deconvolution can be found in Fig. S22 and in Table 5). Comparing the Pd oxidation state of fresh samples and samples at 675 °C (Table 5) shows that the fraction of highly oxidized Pd species remained almost constant throughout the methane oxidation test. However, it is interesting to note that in Pd/Ce100 a substantial fraction of Pd^{2+} ions was reduced mostly to PdO_x and to a lesser extent to metallic palladium, as a result of heating in reaction conditions. The situation markedly changed just adding a small amount of praseodymium. Indeed, by comparing the oxidation state of the fresh and the medium temperature Pd/Ce90Pr10 sample, a decrease in the Pd^{2+} concentration was barely detected; at the same time, a reduction of some PdO_x species to metallic Pd was noted. A similar behavior was also observed for the samples with a higher Pr loading, but with a smaller amount of PdO_x reduced to Pd^0. Hence, in Pd/Ce100 a transformation of Pd^{2+} into more reduced species was observed during CH_4 oxidation, especially approaching the PdO-to-Pd transitional temperature. Instead, in the doped samples praseodymium strongly influences the Pd oxidation state: the fraction of Pd^{2+} was almost unchanged comparing the fresh and the used Pr-containing samples, while only a small amount of PdO_x species weakly bonded to the support were reduced to the metallic form. Thus, these *ex situ* XPS analyses confirm the strong PdO-PrO_x interactions detected throughout the work, which also occur in the presence of water.

Table 5. Relative abundance (at%) of Pd species in the fresh samples and in spent samples resulting from *ex situ* XPS analysis performed in the breakpoints shown in Fig. S21. The corresponding XPS spectra are illustrated in Fig. S22.

Temperature Effect →

Pr Effect ↓

Catalyst	**Palladium species (at%)**							
	Fresh samples				**Wet CH_4 oxidation @ 675 °C**			
	Pd^0	PdO_x	Pd^{2+}	$Pd^{(2+\delta)+}$	Pd^0	PdO_x	Pd^{2+}	$Pd^{(2+\delta)+}$
Pd/Ce100	18.3	37.4	32.2	12.1	21.1	41.2	25.5	12.2
Pd/Ce90Pr10	7.9	23.7	48.4	20.0	15.6	17.7	48.0	18.7
Pd/Ce75Pr25	0.9	18.3	59.1	21.7	3.8	16.3	58.3	21.7
Pd/Ce50Pr50	0.7	15.8	60.1	23.4	2.8	15.3	58.6	23.4
Pd/Pr100	0.0	15.4	60.8	23.8	1.6	15.1	59.2	24.1

In addition, further *ex situ* XPS analyses were performed on Pd/Ce90Pr10, as it is the most active catalyst, in order to investigate the evolution of the Pd oxidation state during dry and wet methane oxidation. In details, the four breakpoints in Fig. 10a and Fig. 10b were examined: the Pd XP spectra corresponding to such points are shown in Fig. S23, while the relative deconvolution results are reported in Table 6. The effect of water on the palladium oxidation state can be evaluated by comparing points 1 and 3 in Fig. 10. At 900 °C, the fraction of metallic Pd in the Pd/Ce90Pr10 sample is much higher in the presence of water. Hence, in wet conditions, a greater fraction of Pd species is involved in the high temperature redox transition. Furthermore, two additional points were considered for the wet methane oxidation cycle (Fig. 10b): point 4 matches the temperature of the minimum conversion achieved during the loss of activity in the cooling cycle (around 675 °C), while point 2 was taken at the same temperature but in the heating phase. In this case, it is noteworthy that the fraction of oxidized palladium species gradually decreases while warming up the system (point 2), until reaching a minimum at the end of the heating cycle (point 3). Moreover, at intermediate temperature (675 °C) a greater percentage of metallic palladium was detected in the cooling ramp (point 4) with respect to the heating one (point 2), thus pointing out the difficult palladium oxidation occurring in the cooling phase. In this respect, the limited ability to re-form palladium oxide during the cooling ramp was ascribed to kinetic limitations [43]. Overall, the results obtained from *ex situ* XPS indicate that Pd oxidation state changes in a significant way during the wet CH_4 oxidation. Additionally, in water presence, the amount of palladium species taking part in the redox transformation at high temperature is greater compared to the dry cycle.

In the final analysis, the water deactivation effect turns out to be a complex phenomenon influenced by both effects studied so far, that is, water adsorption and Pd oxidation state alteration. Among the studied samples, Pd/Ce90Pr10 sample appears to be the most active catalyst either in the absence or presence of water. Although a higher palladium fraction is involved in the redox transformation during the reaction cycle in wet conditions (compared to the dry one), the competitive adsorption between the water and the methane molecules could be substantially reduced thanks to the hydrophobicity of this catalytic system, thus promoting the methane-catalyst interactions. Moreover, the surface OH groups, whether they are produced by the CH_4 oxidation reaction (dry conditions) or by the presence of water in the inlet flow (wet conditions), are retained to a lesser extent from the catalytic surface, thereby allowing a quick regeneration of the active sites.

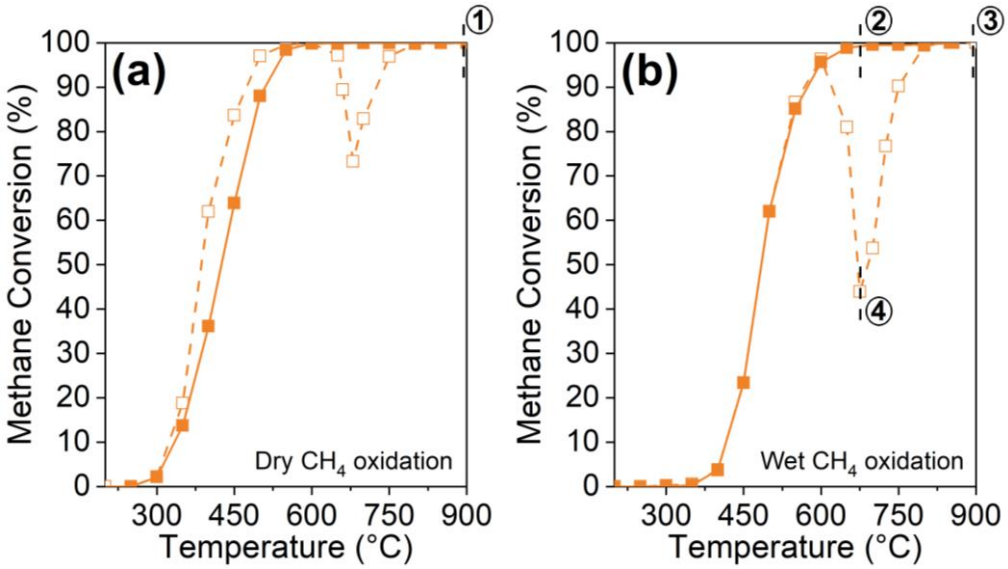

Fig. 10. Dry (a) and wet (b) breakpoints during the CH_4 oxidation reaction. For each point, *ex situ* XPS analyses were carried out to study the Pd chemical state (Table 5).

Table 6. Relative abundance (at%) of palladium species in Pd/Ce90Pr10 resulting from the *ex situ* XPS analysis performed in the breakpoints shown in Fig. 10.

CH_4 oxidation breakpoints	**Palladium species (at%)**			
	Pd^0	**PdO_x**	**Pd^{2+}**	**$Pd^{(2+\delta)+}$**
① Pd/Ce90Pr10 DRY @ 900 °C	17.7	20.5	41.8	20.0
② Pd/Ce90Pr10 WET @ 675 °C Heating	15.6	17.7	48.0	18.7
③ Pd/Ce90Pr10 WET @ 900 °C	33.4	23.8	23.7	19.2
④ Pd/Ce90Pr10 WET @ 675 °C Cooling	22.3	20.5	37.9	19.4

Finally, for comprehensively studying the Pd/Ce90Pr10 catalyst, its long-term stability in wet conditions was assessed at two different temperatures (i.e. two different levels of conversion). More specifically, after performing a first methane oxidation cycle, the second run was blocked at the temperature of interest for several hours. Interestingly, the activity of Pd/Ce90Pr10 was well preserved treating the sample at both 500 °C for 3 h (CH_4 conversion of 60% – see Fig. S24) and 565 °C for 8 h (CH_4 conversion of 90% – see Fig. S25). Hence, this catalyst is characterized by a high thermal stability and the water inhibition effect does not affect its long-term performances above 500 °C. The palladium oxidation state of the used catalyst was determined by using *ex situ* XPS analysis, through the same procedure previously described. By comparing the deconvolution results of the fresh and spent samples (see Table 2, Fig. S26 and Table S17), the percentage of $Pd^{(2+\delta)+}$ was unchanged. On the other hand, in both the exhausted samples the metallic palladium slightly increased compared to the Pd^0 percentage detected in the fresh material. This means that a small amount of oxidized palladium was reduced during the stability test. However, most interestingly, a decrease in the PdO amount associated with an increase in the PdO_x concentration is clearly noticeable in the used samples as compared with the fresh one, especially for the sample tested at a higher temperature. As anticipated in the XPS section, the formation of a substantial amount of PdO_x was expected, looking at its pivotal role as a redox transitional compound in the reduction of palladium oxide to metallic palladium. Moreover, the palladium oxidation transition from oxidized PdO to intermediate PdO_x species was not related neither to a decrease in the catalytic activity nor to a change in the Pd morphology (Figs. S25 and S28). Hence, the high hydrothermal stability of Pd/Ce90Pr10 makes this catalyst a promising candidate for real applications.

4. Conclusions

In summary, nanostructured ceria, ceria-praseodymia and praseodymia catalysts synthesized through the hydrothermal method and impregnated with 2 wt% of Pd were fully characterized and tested for dry and wet complete CH_4 oxidation.

The introduction of a small amount of Pr into the ceria structure allows to obtain a more active material (2 wt% of Pd supported on a mixed oxide with 10% of Pr) than the typical Pd/CeO_2 systems. Hence, the simultaneous presence of Pd in its reduced and oxidized forms, detected by XPS, turned out to be a key factor for high activity. On the other hand, the catalytic activity decreases when further increasing the Pr content due to the palladium retention mainly in its oxidized form. Overall, a large amount of Pr turns out beneficial to reducing the activity loss at 650 – 700 °C due to the PdO-Pd transition observed in the catalytic tests, but also disadvantageous in terms of low-temperature activity. This behaviour arises from strong interactions between the Pd and Pr oxides, confirmed by the formation of a $PdO\text{-}PrO_x$ mixed-phase observed via XRD, HRTEM and Raman analyses.

Additionally, our results provide compelling evidence of the high activity and stability of Pd/Ce90Pr10 also in the presence of water, considering its greatest hydrophobicity detected through *in situ* FTIR and NMR analyses, paving the way for using this system in real applications.

Declaration of Competing Interest

The authors declare that they have no known competing financial interests or personal relationships that could have appeared to influence the work reported in this paper.

Acknowledgments

The authors wish to thank the work of Camilla Galletti for XRD measurements, Mauro Raimondo for FESEM images, Salvatore Guastella for XPS spectra and Maria Carmen Valsania for the acquisition of additional HRTEM images. We also thank Elena Valli and Laura De Vittorio for their thesis work.

References

[1] K. Murata, D. Kosuge, J. Ohyama, Y. Mahara, Y. Yamamoto, S. Arai, A. Satsuma, Exploiting Metal-Support Interactions to Tune the Redox Properties of Supported Pd Catalysts for Methane Combustion, ACS Catal. 10 (2020) 1381–1387. https://doi.org/10.1021/acscatal.9b04524.

[2] S. Chen, S. Li, R. You, Z. Guo, F. Wang, G. Li, W. Yuan, B. Zhu, Y. Gao, Z. Zhang, H. Yang, Y. Wang, Elucidation of active sites for CH_4 catalytic oxidation over Pd/CeO_2 via tailoring metal−support interactions, ACS Catal. 11 (2021) 5666–5677. https://doi.org/10.1021/acscatal.1c00839.

[3] S. Colussi, P. Fornasiero, A. Trovarelli, Structure-activity relationship in Pd/CeO_2 methane oxidation catalysts, Chinese J. Catal. 41 (2020) 938–950. https://doi.org/10.1016/S1872-2067(19)63510-2.

[4] M. Cargnello, J.J. Delgado Jaén, J.C. Hernández Garrido, K. Bakhmutsky, T. Montini, J.J. Calvino Gámez, R.J. Gorte, P. Fornasiero, Exceptional activity for methane combustion over modular $Pd@CeO_2$ subunits on functionalized Al2O3, Science. 337 (2012) 713–717. https://doi.org/10.1126/science.1222887.

[5] S. Zhang, C. Chen, M. Cargnello, P. Fornasiero, R.J. Gorte, G.W. Graham, X. Pan, Dynamic structural evolution of supported palladium-ceria core-shell catalysts revealed by in situ electron microscopy, Nat. Commun. 6 (2015) 1–6. https://doi.org/10.1038/ncomms8778.

[6] M. Danielis, L.E. Betancourt, I. Orozco, N.J. Divins, J. Llorca, J.A. Rodríguez, S.D. Senanayake, S. Colussi, A. Trovarelli, Methane oxidation activity and nanoscale characterization of Pd/CeO_2 catalysts prepared by dry milling Pd acetate and ceria, Appl. Catal. B Environ. 282 (2021) 119567. https://doi.org/10.1016/j.apcatb.2020.119567.

[7] W. Huang, A.C. Johnston-Peck, T. Wolter, W.C.D. Yang, L. Xu, J. Oh, B.A. Reeves, C. Zhou, M.E. Holtz, A.A. Herzing, A.M. Lindenberg, M. Mavrikakis, M. Cargnello, Steam-created grain boundaries for methane C–H activation in palladium catalysts, Science. 373 (2021) 1518–1523. https://doi.org/10.1126/science.abj5291.

[8] K. Persson, L.D. Pfefferle, W. Schwartz, A. Ersson, S.G. Järås, Stability of palladium-based catalysts during catalytic combustion of methane: The influence of water, Appl. Catal. B Environ. 74 (2007) 242–250. https://doi.org/10.1016/j.apcatb.2007.02.015.

[9] R. Burch, F.J. Urbano, P.K. Loader, Methane combustion over palladium catalysts: The effect of carbon dioxide and water on activity, Appl. Catal. A, Gen. 123 (1995) 173–184. https://doi.org/10.1016/0926-860X(94)00251-7.

[10] R. Gholami, M. Alyani, K.J. Smith, Deactivation of Pd catalysts by water during low temperature methane oxidation relevant to natural gas vehicle converters, 2015. https://doi.org/10.3390/catal5020561.

[11] D. Ciuparu, E. Perkins, L. Pfefferle, In situ DR-FTIR investigation of surface hydroxyls on γ-Al_2O_3 supported PdO catalysts during methane combustion, Appl. Catal. A Gen. 263 (2004) 145–153. https://doi.org/10.1016/j.apcata.2003.12.006.

[12] W.R. Schwartz, D. Ciuparu, L.D. Pfefferle, Combustion of methane over palladium-based catalysts: Catalytic deactivation and role of the support, J. Phys. Chem. C. 116 (2012) 8587–8593. https://doi.org/10.1021/jp212236e.

[13] R. Burch, Low NO_x options in catalytic combustion and emission control, Catal. Today. 35 (1997) 27–36. https://doi.org/10.1016/S0920-5861(96)00131-9.

[14] W. Huang, E.D. Goodman, P. Losch, M. Cargnello, Deconvoluting Transient Water Effects on the Activity of Pd Methane Combustion Catalysts, Ind. Eng. Chem. Res. 57 (2018) 10261–10268. https://doi.org/10.1021/acs.iecr.8b01915.

[15] W. Huang, X. Zhang, A.C. Yang, E.D. Goodman, K.C. Kao, M. Cargnello, Enhanced Catalytic Activity for Methane Combustion through in Situ Water Sorption, ACS Catal. 10 (2020) 8157–8167. https://doi.org/10.1021/acscatal.0c02087.

[16] T. Andana, M. Piumetti, S. Bensaid, L. Veyre, C. Thieuleux, N. Russo, D. Fino, E.A. Quadrelli, R. Pirone, Nanostructured equimolar ceria-praseodymia for NO_x-assisted soot oxidation: Insight into Pr dominance over Pt

nanoparticles and metal–support interaction, Appl. Catal. B Environ. 226 (2018) 147–161. https://doi.org/10.1016/j.apcatb.2017.12.048.

[17] S. Ballauri, E. Sartoretti, C. Novara, F. Giorgis, M. Piumetti, D. Fino, N. Russo, S. Bensaid, Wide range temperature stability of palladium on ceria-praseodymia catalysts for complete methane oxidation, Catal. Today. (2021). https://doi.org/10.1016/j.cattod.2021.11.035.

[18] E. Fukushima, S.B.W. Roeder, Experimental Pulse NMR: A Nuts and Bolts Approach, 1981.

[19] H.Y. Carr, E.M. Purcell, Effects of diffusion on free precession in nuclear magnetic resonance experiments, Phys. Rev. 94 (1954) 630–638. https://doi.org/10.1103/PhysRev.94.630.

[20] T. Andana, M. Piumetti, S. Bensaid, N. Russo, D. Fino, Heterogeneous mechanism of NO_x-assisted soot oxidation in the passive regeneration of a bench-scale diesel particulate filter catalyzed with nanostructured equimolar ceria-praseodymia, Appl. Catal. A Gen. 583 (2019) 117136. https://doi.org/10.1016/j.apcata.2019.117136.

[21] M. Piumetti, S. Bensaid, T. Andana, M. Dosa, C. Novara, F. Giorgis, N. Russo, D. Fino, Nanostructured ceria-based materials: Effect of the hydrothermal synthesis conditions on the structural properties and catalytic activity, Catalysts. 7 (2017). https://doi.org/10.3390/catal7060174.

[22] T.C. Chou, T. Kennelly, R.J. Farrauto, US Patent 5 169 300: Praseodymium-palladium binary oxide, catalyst, methods of combustion and regeneration, 1992.

[23] V.A. Sadykov, Y. V. Frolova, G.M. Alikina, A.I. Lukashevich, V.S. Muzykantov, V.A. Rogov, E.M. Moroz, D.A. Zyuzin, V.P. Ivanov, H. Borchert, E.A. Paukshtis, V.I. Bukhtiyarov, V. V. Kaichev, S. Neophytides, E. Kemnitz, K. Scheurell, Mobility and reactivity of the lattice oxygen of Pr-doped ceria promoted with Pt, React. Kinet. Catal. Lett. 86 (2005) 21–28. https://doi.org/10.1007/s11144-005-0290-6.

[24] E. Sartoretti, C. Novara, F. Giorgis, M. Piumetti, S. Bensaid, N. Russo, D. Fino, In situ Raman analyses of the soot oxidation reaction over nanostructured ceria-based catalysts, Sci. Rep. 9 (2019) 3875. https://doi.org/10.1038/s41598-019-39105-5.

[25] E. Sartoretti, C. Novara, A. Chiodoni, F. Giorgis, M. Piumetti, S. Bensaid, N. Russo, D. Fino, Nanostructured ceria-based catalysts doped with La and Nd: How acid-base sites and redox properties determine the oxidation mechanisms, Catal. Today. (2022). https://doi.org/10.1016/J.CATTOD.2021.11.040.

[26] E. Sartoretti, C. Novara, M. Fontana, F. Giorgis, M. Piumetti, S. Bensaid, N. Russo, D. Fino, New insights on the defect sites evolution during CO oxidation over doped ceria nanocatalysts probed by in situ Raman spectroscopy, Appl. Catal. A Gen. 596 (2020) 117517. https://doi.org/10.1016/j.apcata.2020.117517.

[27] A. Westermann, C. Geantet, P. Vernoux, S. Loridant, Defects band enhanced by resonance Raman effect in praseodymium doped CeO_2, J. Raman Spectrosc. 47 (2016) 1276–1279. https://doi.org/10.1002/jrs.4943.

[28] A. Baylet, P. Marécot, D. Duprez, P. Castellazzi, G. Groppi, P. Forzatti, In situ Raman and in situ XRD analysis of PdO reduction and Pd° oxidation supported on γ-Al_2O_3 catalyst under different atmospheres, Phys. Chem. Chem. Phys. 13 (2011) 4607–4613. https://doi.org/10.1039/c0cp01331e.

[29] A. Trovarelli, J. Llorca, Ceria Catalysts at Nanoscale: How Do Crystal Shapes Shape Catalysis?, ACS Catal. 7 (2017) 4716–4735. https://doi.org/10.1021/acscatal.7b01246.

[30] J.G. Kang, B.K. Min, Y. Sohn, Physicochemical properties of praseodymium hydroxide and oxide nanorods, J. Alloys Compd. 619 (2015) 165–171. https://doi.org/10.1016/j.jallcom.2014.09.059.

[31] X. Garcia, L. Soler, N.J. Divins, X. Vendrell, I. Serrano, I. Lucentini, J. Prat, E. Solano, M. Tallarida, C. Escudero, J. Llorca, Ceria-based catalysts studied by near ambient pressure x-ray photoelectron spectroscopy: A review, Catalysts. 10 (2020). https://doi.org/10.3390/catal10030286.

[32] Y. Zhang, J. Deng, H. Zhang, Y. Liu, H. Dai, Three-dimensionally ordered macroporous Pr_6O_{11} and Tb_4O_7 with mesoporous walls: Preparation, characterization, and catalytic activity for CO oxidation, Catal. Today. 245 (2015) 28–36. https://doi.org/10.1016/j.cattod.2014.09.017.

[33] D. Mandal, K.J. Kim, J.S. Lee, Simple synthesis of palladium nanoparticles, β-phase formation, and the control of chain and dipole orientations in palladium-doped poly(vinylidene fluoride) thin films, Langmuir. 28 (2012) 10310–10317. https://doi.org/10.1021/la300983x.

[34] E. Sartoretti, F. Martini, M. Piumetti, S. Bensaid, N. Russo, D. Fino, Nanostructured Equimolar Ceria-Praseodymia for Total Oxidations in Low-O_2 Conditions, Catalysts. 10 (2020) 1–16. https://doi.org/10.3390/catal10020165.

[35] S. Colussi, A. Gayen, M. Boaro, J. Llorca, A. Trovarelli, Influence of Different Palladium Precursors on the

Properties of Solution-Combustion-Synthesized Palladium/Ceria Catalysts for Methane Combustion, 700032

[36] S. Colussi, A. Trovarelli, E. Vesselli, A. Baraldi, G. Comelli, G. Groppi, J. Llorca, Structure and morphology of Pd/Al_2O_3 and $Pd/CeO_2/Al_2O_3$ combustion catalysts in Pd-PdO transformation hysteresis, Appl. Catal. A Gen. 390 (2010) 1–10. https://doi.org/10.1016/j.apcata.2010.09.033.

[37] R.J. Farrauto, M.C. Hobson, T. Kennelly, E.M. Waterman, Catalytic chemistry of supported palladium for combustion of methane, Appl. Catal. A, Gen. 81 (1992) 227–237. https://doi.org/10.1016/0926-860X(92)80095-T.

[38] R. V. Gulyaev, A.I. Stadnichenko, E.M. Slavinskaya, A.S. Ivanova, S. V. Koscheev, A.I. Boronin, In situ preparation and investigation of Pd/CeO_2 catalysts for the low-temperature oxidation of CO, Appl. Catal. A Gen. 439–440 (2012) 41–50. https://doi.org/10.1016/j.apcata.2012.06.045.

[39] D. Mukherjee, B.G. Rao, B.M. Reddy, CO and soot oxidation activity of doped ceria: Influence of dopants, Appl. Catal. B Environ. 197 (2016) 105–115. https://doi.org/10.1016/j.apcatb.2016.03.042.

[40] A. Toso, S. Colussi, S. Padigapaty, C. de Leitenburg, A. Trovarelli, High stability and activity of solution combustion synthesized Pd-based catalysts for methane combustion in presence of water, Appl. Catal. B Environ. 230 (2018) 237–245. https://doi.org/10.1016/j.apcatb.2018.02.049.

[41] W. Chun, G.W. Graham, J.A. Lupescu, R.W. McCabe, M.M. Koranne, R. Brezny, Reducibility of catalyzed cerium-praseodymium mixed oxides, Catal. Letters. 106 (2006) 95–100. https://doi.org/10.1007/s10562-005-9613-5.

[42] V. Ferrer, A. Moronta, J. Sánchez, R. Solano, S. Bernal, D. Finol, Effect of the reduction temperature on the catalytic activity of Pd-supported catalysts, Catal. Today. 107–108 (2005) 487–492. https://doi.org/10.1016/j.cattod.2005.07.059.

[43] M. Monai, T. Montini, C. Chen, E. Fonda, R.J. Gorte, P. Fornasiero, Methane Catalytic Combustion over Hierarchical $Pd@CeO_2/Si\text{-}Al_2O_3$: Effect of the Presence of Water, ChemCatChem. 7 (2015) 2038–2046. https://doi.org/10.1002/cctc.201402717.

[44] S. Agarwal, X. Zhu, E.J.M. Hensen, L. Lefferts, B.L. Mojet, Defect chemistry of ceria nanorods, J. Phys. Chem. C. 118 (2014) 4131–4142. https://doi.org/10.1021/jp409989y.

[45] C. D'Agostino, J. Mitchell, M.D. Mantle, L.F. Gladden, Interpretation of NMR relaxation as a tool for characterising the adsorption strength of liquids inside porous materials, Chem. - A Eur. J. 20 (2014) 13009–13015. https://doi.org/10.1002/chem.201403139.

[46] C. D'Agostino, M.D. Mantle, L.F. Gladden, In situ high-pressure $^{13}C/^{1}H$ NMR reaction studies of benzyl alcohol oxidation over a Pd/Al_2O_3 catalyst, React. Chem. Eng. 5 (2020) 1053–1057. https://doi.org/10.1039/c9re00489k.

[47] K. Ralphs, C. D'Agostino, R. Burch, S. Chansai, L.F. Gladden, C. Hardacre, S.L. James, J. Mitchell, S.F.R. Taylor, Assessing the surface modifications following the mechanochemical preparation of a Ag/Al_2O_3 selective catalytic reduction catalyst, Catal. Sci. Technol. 4 (2014) 531–539. https://doi.org/10.1039/c3cy00945a.

[48] C. D'Agostino, M.R. Feaviour, G.L. Brett, J. Mitchell, A.P.E. York, G.J. Hutchings, M.D. Mantle, L.F. Gladden, Solvent inhibition in the liquid-phase catalytic oxidation of 1,4-butanediol: Understanding the catalyst behaviour from NMR relaxation time measurements, Catal. Sci. Technol. 6 (2016) 7896–7901. https://doi.org/10.1039/c6cy01458e.

[49] J.J. Willis, A. Gallo, D. Sokaras, H. Aljama, S.H. Nowak, E.D. Goodman, L. Wu, C.J. Tassone, T.F. Jaramillo, F. Abild-Pedersen, M. Cargnello, Systematic Structure-Property Relationship Studies in Palladium-Catalyzed Methane Complete Combustion, ACS Catal. 7 (2017) 7810–7821. https://doi.org/10.1021/acscatal.7b02414.

[50] Y. Xin, S. Lieb, H. Wang, C.K. Law, Kinetics of Catalytic Oxidation of Methane over Palladium Oxide by Wire Microcalorimetry, J. Phys. Chem. C. 117 (2013) 19449–19507. https://doi.org/10.1016/j.proci.2014.06.094.